COVID-19 Neuropathology: evidence for SARS-CoV-2 invasion of Human Brainstem Nuclei

Abstract

Neurological manifestations are common in COVID-19, the disease caused by SARS-CoV-2. Despite reports of SARS-CoV-2 detection in the brain and cerebrospinal fluid of COVID-19 patients, it's still unclear whether the virus can infect the central nervous system, and which neuropathological alterations can be ascribed to viral tropism, rather than immune-mediated mechanisms.

Here, we assess neuropathological alterations in 24 COVID-19 patients and 18 matched controls who died due to pneumonia / respiratory failure. Aside from a wide spectrum of neuropathological alterations, SARS-CoV-2-immunoreactive neurons were detected in specific brainstem nuclei of 5 COVID-19 subjects. Viral RNA was also detected by real-time RT-PCR. Quantification of reactive microglia revealed an anatomically segregated pattern of inflammation within affected brainstem regions, and was higher when compared to controls. While the results of this study support the neuroinvasive potential of SARS-CoV-2, the role of SARS-CoV-2 neurotropism in COVID-19 and its long-term sequelae require further investigation.

Introduction

Neurological manifestations are common in coronavirus disease 19 (COVID-19), the disease caused by severe acute respiratory syndrome coronavirus-2 (SARS-CoV-2)[1-5]. Symptoms range from anosmia, ageusia, dizziness and headache, which are commonly reported by patients with mild disease, to altered mental status, neuropsychiatric disorders, stroke, and, rarely, meningitis, encephalitis, and polyneuritis, which occur in hospitalized patients with severe disease[1,5]. Between 10 to 30% of people with SARS-CoV-2 infection experience long-term sequelae, referred as “long COVID”, including neurological manifestations such as hyposmia, hypogeusia, headaches, fatigue, sleep disorders, pain, and cognitive impairment[3]. Despite some reports of detection of SARS-CoV-2 in the brain and cerebrospinal fluid of patients with COVID-19[2-3,6], it is still unclear whether the virus can infect the central nervous system (CNS). In particular, it still remains to be elucidated whether neurological manifestations and neural damage are a direct consequence of viral invasion of the CNS, are due to post-infectious immune-mediated disease, or are the result of systemic disease[1,6-11]. Studies on human neural cell cultures and brain organoids report conflicting data on SARS-CoV-2 neurotropism[12]. Overall, they suggest that SARS-CoV-2 does not infect and replicate efficiently in human neural cells, while it can replicate at high rates in choroid plexus epithelial cells[7,13-14]. At variance, intranasal inoculation of SARS-CoV-2 in transgenic mice overexpressing human ACE2 under the K18 promoter resulted in brain invasion and widespread infection of neurons, radial glia and neuronal progenitor cells[15-16]. Other coronaviruses, such as SARS-CoV and MERS-CoV, appear to be able to infect the CNS in both humans and animal models[17].

Data deriving from large autopsy studies in patients who died from COVID-19 suggest for the neuroinvasive potential of SARS-CoV-2 in the CNS[8-9,17], even though infection appears to be limited to sparse cells in the brainstem and not associated with encephalitis or other

specific changes referable to the virus[8]. Conversely, other studies failed to detect SARS-CoV-2 antigens or genomic sequences in brain tissues of COVID-19 patients[11,17-18,37-38]. In numerous instances, neuropathological changes in the brains of COVID-19 patients were moderate and mainly represented by ischaemic lesions, astrogliosis, microglial nodules, and cytotoxic T lymphocyte infiltrates, most pronounced in the brainstem, cerebellum, and meninges[8-9,11,18,21]. While diffuse to focal hypoxic / ischaemic damage was a common finding in COVID-19 patients across studies, no direct link between encountered neuropathological alterations and direct viral invasion could be established, with systemic inflammation and hypoxia playing a likely major role in mediating brain immune response[37]. Single-nucleus gene-expression profiling of frontal cortex and choroid plexus tissues from severe COVID-19 patients showed broad perturbations, with upregulation of genes involved in innate antiviral response and inflammation, microglia activation and neurodegeneration[20], but no direct evidence of viral tropism was found; similarly, Fullard et al.[38] were unable to detect viral transcripts and S proteins in different brain regions of COVID-19 subjects. Deep spatial profiling of the local immune response in COVID-19 brains through imaging mass spectrometry revealed significant immune activation in the CNS with pronounced neuropathological changes (astrocytosis, axonal damage, and blood-brain-barrier leakage) and detected viral antigen in ACE2-positive cells enriched in the vascular compartment[18]. According to the study, the presence of viral antigen was linked to vascular proximity and ACE2 expression, while also being correlated to the perivascular immune activation patterns of CD8 and CD4 T cells and myeloid- and microglial-cell subsets[18], indicating a fundamental role of the vascular and perivascular compartment, as well as Blood-brain-barrier impairment, in mediating COVID-19 specific neuropathological changes. As evidenced by the above case series, and considering the different case reports available[22-24], SARS-CoV-2 infection of CNS seems to be limited to isolated cells within the perivascular compartment of the brainstem and olfactory bulb, and have been reported in a subset of cases in the

various autopsy series, while widespread neuropathological sequelae (such as astrogliosis, microgliosis, lymphocyte infiltration, microvascular injury, fibrinogen leakage) have been documented in most examined specimens. The possibility of direct viral invasion, and eventual associated long-term sequelae of infection, remain to be investigated.

In the present study, we assess the neuropathological changes of 24 patients who died following a diagnosis of SARS-CoV-2 infection in Italy during the COVID-19 pandemic (from March 2020 to May 2021) and 18 age-matched controls with comparable medical conditions who died mainly due to pneumonia and / or respiratory failure.

Study design and Materials

Hospitalized patients who died following a diagnosis of SARS-CoV-2 infection in the Veneto Region, Italy, during the peak incidence of COVID-19 (from March 2020 to May 2021) were autopsied according to established COVID-19 infection security protocols. Inclusion criteria for the study were: a) diagnosis of SARS-CoV-2 infection confirmed by molecular testing of rhino-pharyngeal swabs and b) high-quality brain tissue samples available for histopathological and immunohistochemical analysis. Tissue quality was determined by Post-Mortem Interval (PMI) ≤5 days, absence of tissue maceration, fixation time ≤ 3 weeks and adequate formalin penetration within the tissue. A total of 24 COVID-19 patients were included in the study.

18 age- and sex-matched subjects with comparable general medical conditions, predating the COVID-19 pandemic in Italy, were included as controls.

Methods

Clinical information. Available clinical data for COVID-19 subjects and controls were examined, including ante-mortem medical history, neurological and neuroradiological findings, hospitalization time, ICU and oxygen therapy status, and prescribed medication.

However, as most subjects died during the sanitary emergency of the first wave of the COVID-19 pandemic in Italy, ante-mortem clinical data were at times limited, especially when concerning post-hospitalization neurological status. This represents one of the main limitations of our study, determining significant constrains to the association between ante-mortem neurological findings and encountered neuropathological alterations, which is often not unequivocal.

Sampling and fixation procedures. Sampled brains were immersion fixed in 4% phosphate-buffered formalin solution following autopsy (mean PMI: 3 days; Range 0-5 days; average fixation time: 2-3 weeks) and subsequently sectioned for histopathological and immunohistochemical analysis. Samples of the cerebral cortex, basal ganglia, hippocampus, cerebellar cortex, deep cerebellar nuclei, choroid plexuses and meninges were obtained, while the brainstem was isolated at the level of the rostral extremity of the midbrain and extensively sampled in its whole cranio-caudal extent. The 12 cranial nerves, where available, including the olfactory bulb, tract and bifurcation, were also sampled. To preserve antigen quality, a slow dehydration and clearing protocol was performed prior to paraffin embedding (24h mean tissue processing time).

Histochemical and immunoperoxidase staining. Haematoxylin and Eosin staining was employed for routine histopathological evaluation. Immunoperoxidase staining was performed on a Dako EnVision Autostainer (Dako Denmark A/S, Glostrup, Denmark) according to manufacturer recommendations. Antibodies for CD3 (Polyclonal Rabbit Anti-Human, Citrate Buffer HIER, dilution 1:200, Dako Omnis, Code Number: GA503), CD20 (Monoclonal Mouse Anti-Human, Citrate Buffer HIER, dilution 1:200 Clone KP1, Dako Omnis, Code Number: M0814) and CD68 (Monoclonal Mouse Anti-Human, EDTA Buffer HIER, IHC dilution 1:5000, IF dilution 1:500, Clone L26, Dako Omnis, Code Number: M0756) were employed to characterize lympho-monocytic infiltrations. Microglial Activation was

assessed using both CD68 (as above), HLA-DR Antibody (Monoclonal Rabbit Anti-Human, Citrate Buffer HIER, dilution 1:50 Clone: LN-3, Invitrogen, Thermo Fisher Scientific, Waltham, MA, USA), TMEM119 (Rabbit Anti-Human, Citrate Buffer HIER, dilution 1:250, Abcam, Code Number: ab185333), while microglial proliferation was assessed using anti-Ki-67 immunohistochemistry (Mouse Anti-Human, EDTA Buffer HIER, dilution 1:200, Spring Bioscience, Code number: M3060). Anti-GFAP immunohistochemistry (Polyclonal Rabbit Anti-Human, Proteinase K enzymatic antigen retrieval, dilution 1:1000, DAKO Omnis, Code Number: GA524) was employed to assess reactive astrogliosis. Anti-CD61 immunohistochemistry (Monoclonal Mouse Anti-Human, Citrate Buffer HIER, dilution 1:75, Clone Y2/51, Dako Omnis, Code Number: M0753) was also employed to evaluate the presence of platelet-enriched microthrombi. Anti-SARS-CoV-2 nucleocapsid (Rabbit Anti-Human, Citrate Buffer HIER, dilution 1:7000, Sino Biologicals, 40143-R001) and -Spike Subunit 1 Antibody (Monoclonal Rabbit Anti-Human, Citrate Buffer HIER, dilution 1:100, Clone 007, Sino Biological, Code Number: 40150-R007) immunostainings were employed to evaluate viral antigens within the tissue. The expression of ACE2 Receptor protein (Rabbit Anti-Human Polyclonal, Citrate Buffer HIER, dilution 1:2000, Abcam, Code Number: ab15348) and TMPRSS-2 protein (Rabbit Anti-Human Monoclonal, Citrate Buffer HIER, dilution 1:2500, Abcam, Code Number: ab242384) was assessed within the brainstem and cerebellum, and in all sections with positive findings for viral proteins. Anti-nucleocapsid and anti-spike antibodies were validated through SARS-CoV-2 infected Vero E6 cells and autopsy-derived lung tissue from SARS-CoV-2 infected patients as positive controls; non-infected cells and lung sections deriving from autopsy cases predating COVID-19 pandemic (2017) were used as negative controls (Supplementary Figure 1). Peroxidase reactions were repeated at least three times to ensure reaction consistency.

Immunofluorescent staining and confocal microscopy. Fluorescent immunohistochemistry was performed manually. Antigen retrieval was performed on de-paraffinized tissue sections using Dako EnVision PTLink station according to manufacturer recommendations. Following antigen retrieval, autofluorescence was quenched with a 50 mM NH_4Cl solution for 10 minutes. Sections were treated with permeabilization and blocking solution (15% vol/vol Goat Serum, 2% wt/vol BSA, 0.25% wt/vol gelatin, 0.2% wt/vol glycine in PBS) containing 0.5% Triton X-100 for 90 minutes before primary antibody incubation. The following antibodies were employed: CD68 (#M0756; 1:500); TMEM119 (#ab185333; 1:200); Ki-67 (#M3060; 1:200); β-III Tubulin (#T8578; 1:300); Tyrosine Hydroxylase (#T2928; 1:6000); SARS-CoV-2 Nucleocapsid Protein (#40143-R001; 1:3000); SARS-CoV-2 Spike Subunit 1 Protein (#40150-R007; 1:100); ACE2 Receptor Protein (#ab15348; 1:500) and TMPRSS-2 (#ab242384; 1:1000). Primary antibodies were diluted in blocking solution and incubated at 4°C overnight. Alexa-Fluor plus 488 Goat anti-Mouse secondary antibody (Code number: A32723) and Alexa-Fluor plus 568 anti-Rabbit secondary antibody (Code number: A-11011) were diluted 1:200 in blocking solution as above and incubated for 60 minutes at room temperature. To further avoid background signal and tissue autofluorescence, slides were incubated for 10 minutes in 0.5% Sudan Black B solution in 70% ethanol at room temperature and abundantly washed with PBS, followed by Hoechst 33258 nuclear staining (Invitrogen, dilution: 1:10000 in PBS) for 10 minutes. Slides were mounted and coverslipped with Mowiol solution (prepared with Mowiol 4-88 reagent, MerckMillipore, Code number: 475904-100GM). Confocal immunofluorescence z-stack images were acquired on a Leica SP5 Laser Scanning Confocal Microscope using a HC PL FLUOTAR 20x/0.50 Dry or HCX PL APO lambda blue 40X/1.40 Oil objectives. Images were acquired at a 16-bit intensity resolution over 2048 × 2048 pixels. Z-stacks images were converted into digital maximum intensity z-projections, processed, and analyzed using ImageJ software.

RT-PCR analyses. Viral RNA analysis was performed on 20µm thick paraffin-embedded sections collected in sterile 2ml Eppendorf vials; disposable microtome blades and tongs were changed for each section to reduce contamination risk. Real-time RT-PCR analyses were performed to detect SARS-CoV-2 genome sequences. Briefly, total RNA was purified from selected material using a RecoverAll™ Total Nucleic Acid Isolation kit (Thermo Fisher Scientific) following the manufacturer's instructions. One-step real-time RT-PCR assays targeting SARS-CoV-2 nucleocapsid (N) coding region and subgenomic RNA were run on ABI 7900HT Sequence Detection Systems (Thermo Fisher Scientific), as previously reported[25].

Histopathological and morphometrical evaluation. Slides were examined by three independent histopathologists and morphologists blind to patient clinical findings and COVID-19 status. Disagreements were resolved by consensus. The degree of brainstem hypoxic / ischaemic damage, astrogliosis and microgliosis were classified using a four-tiered semi-quantitative approach for each evaluated section, while microglial density and activation was assessed by the means of digitally-assisted immunoreactivity quantification by three independent evaluators.

Quantification of Activated Microglia. The degree of microgliosis was assessed through a digitally-assisted quantification approach at the level of the medulla, pons and mesencephalon. For each subject, standard sections passing through the area postrema (medulla), locus coeruleus (pons) and decussation of the superior cerebellar peduncles or red nucleus (midbrain) underwent TMEM119 immunoperoxidase staining and TMEM119 / CD68 double fluorescent immunohistochemistry. TMEM119+ structures with visible nucleus and microglial-compatible morphology were classified as microglial cells, while TMEM119- / CD68+ elements with compatible morphology were classified as monocyte/macrophages. Ramifications and cell processes without a visible nucleus were excluded from our analysis

in order to avoid overestimation of cell densities by including neighboring structures belonging to adjacent sections. Morphometrical evaluation occurred within six counting fields (fields of view, FOV) spanning across the dorsal-to-ventral axis of the sections; FOV boundaries and anatomical landmarks are summarized in Supplementary Table 1 for each level of sectioning. The number of immunoreactivities per mm^2 was calculated for each counting field and assigned to one anatomical compartment (i.e. tegmentum, tectum and basis), based on their topography according to Mai and Paxinos[26]. Comparisons and statistical evaluations were conducted per individual counting field, anatomical compartment and level of section (medulla, pons, midbrain). To assess the degree of lysosomal-activity as a marker for microglia phagocytic activity, CD68 immunoreactive area (expressed as percentage of CD68+ immunoreactive area within a counting field, or A%) for 5 randomly selected counting fields at each level of sectioning was computed through particle analysis of the green fluorescent channel on ImageJ software.

Statistical Analyses. Statistical analyses and visualizations were performed using GraphPad Prism 9. Differences in microglial densities (microglia / mm^2) within subgroups of the COVID-19 cohort in figures 4A, 5A and 6A were analyzed by t tests with Welch's correction. Microglial density between individual counting fields (FOVs) in COVID-19 subjects (Figures 4D, 5D, and 6D), as well as differences between anatomical compartments in COVID-19 subgroups (Figures 4B and 5B) and in COVID-19 versus controls (Figures 2E, 4C, 5B, 6E) were determined by Welch one-way ANOVA tests corrected for Dunnett's multiple comparisons. Correlation matrices in Figures 4E and 7G were computed as Spearman's rho for continuous variables and as point-biserial correlations for nominal – continuous variables. Spearman's rho and linear regression was performed in figure 2F. Further statistical details for each plot can be found in the corresponding figure legend. Throughout the manuscript * indicates $p < 0.05$, ** $p < 0.01$, *** $p < 0.001$ and **** $p < 0.0001$.

Results

The main cause of death in COVID-19 subjects was diffuse alveolar damage. Twenty-four COVID-19 patients were included in our study. In all patients, SARS-CoV-2 RNA was detected by molecular testing in rhino-pharyngeal swabs. Eleven were females, while 13 were males. The mean age of the included subjects was 73±13.7 years. Most included subjects were affected by preexisting chronic medical conditions. Eleven patients (7 female, 4 male) were affected by neurological or neurodegenerative disease prior to SARS-CoV-2 infection. Twenty-three patients were hospitalized prior to death. Patients were hospitalized for 14.5±11.3 days and died 1 to 34 days following admission. Eleven subjects were admitted to the ICU during hospitalization and received intensive oxygen therapy (IOT) (i.e. the administration of supplemental oxygen via nasal cannulae, face masks, or tracheal intubation). Fifteen subjects received antithrombotic therapy during hospitalization and were treated with corticosteroid medication. The available clinical data for our cohort is reported in Table 1.

The main cause of death of the control cohort was respiratory failure and pneumonia, aside from other relevant comorbidities. Eighteen age- and sex-matched subjects with comparable ante-mortem medical conditions were included as controls. All patients were negative for SARS-CoV-2 infection or died prior to the COVID-19 pandemic in Italy. Eight were female, while 10 were male. The mean age of included controls was 72±12 years. The mean hospitalization time was 20±15.6 days. Thirteen patients died due to pneumonia, while the remaining subjects died due to respiratory insufficiency, multiorgan failure or ischaemic heart disease. One patient died due to septic shock. Five patients had a clinical diagnosis of cognitive decline. The available clinical data for the control group are reported in Table 2.

Neuropathological examination

A wide spectrum of neuropathological alterations was detected in both COVID-19 and control subjects. The brains of 20 COVID-19 subjects displayed gross macroscopic abnormalities including mild-to-moderate generalized cerebral atrophy (N=9), diffuse cerebral edema (N=9) and chronic territorial ischaemic injury (N=6). Histopathological evaluation revealed diffuse hypoxic / ischaemic damage as a common finding in the COVID-19 cohort, with most subjects presenting mild-to-moderate diffuse hypoxic / ischaemic damage of the cerebral hemispheres and brainstem (Figure 1C), quantified according a four-tiered semi-quantitative scale (reported in Table 1). Furthermore, acute ischaemic injuries were evident in 5 patients. Small vessels were congested in most subjects with moderate perivascular extravasation at the level of the medulla, pons and deep cerebellar nuclei in 6 cases. Variable degrees of astrogliosis were evident in all subjects in all assessed regions, but were more pronounced at the level of the brainstem, as testified by GFAP staining (Supplementary Figure 3; semi-quantitative evaluation of astrogliosis across brain regions is available in Supplementary Table 2). Alzheimer Disease (AD) neuropathological changes, evaluated according to NIA-AA criteria, as well as Cerebral Amyloid Angiopathy (CAA) were detected in 5 subjects. In one case, Parkinson's Disease neuropathological alterations (i.e. deterioration of the ventrolateral substantia nigra and nigral lewy bodies) were found.

Control subjects presented similar macroscopic and histopathological alterations: mild-to-moderate generalized cerebral atrophy (N=7), mild-to-moderate diffuse cerebral edema (N=11) and chronic territorial ischemic injury (N=7); most subjects who died due to pneumonia or respiratory failure presented variable degrees of diffuse hypoxic / ischaemic damage, with mild to moderate damage of the brainstem being a common finding, similarly to COVID-19 subjects (Figure 1C); individual findings for hypoxic / ischaemic injury are reported in Table 2. Four subjects presented AD neuropathological changes and CAA, with

one subject presenting both AD and Lewy Body Dementia mixed pathology. The macroscopic and histopathological findings of both COVID-19 subjects and controls are reported in Table 1 and Table 2.

CNS platelet-enriched microthrombi in small parenchymal vessels were detected in COVID-19 subjects, but not in controls. Small vessel thromboses were detected in 9 COVID-19 patients at the level of the pons, deep cerebellar nuclei and cerebral cortex, with one patient presenting small vessel thromboses in multiple sites. No CNS or systemic thromboses were detected in controls. In all COVID-19 cases, CD61 immunoperoxidase staining revealed platelet-rich microthrombi in small parenchymal vessels, with no evidence of arachnoid of meningeal vessels being involved, as seen in Figure 1D. Other organs were often affected, such as the lungs, liver, intestine, and hypopharynx and even the carotid body[10,27-28], as summarized in Table 1. In 3 out of 9 cases, microthromboses were identified only within the CNS, while in the remaining 6 subjects, pulmonary thromboses were also detected. Interestingly, 3 out of 9 subjects with CNS microthrombi were on antithrombotic medication, 4 were not actively treated prior to death, and in 2 cases clinical information regarding antithrombotic medication was incomplete. In line with previous findings in literature, CNS microthromboses appear to be peculiar to the COVID-19 cohort, with no control subject presenting either fibrin- or platelet-enriched microthrombi in the CNS or other organs regardless of the cause of death.

Microglial cells with an activated phenotype and frequent microglial nodules were found in COVID-19 subjects, but not in controls. In 23 COVID-19 subjects parenchymal microglia displayed an activated phenotype with characteristic thorny ramifications or amoeboid

297 morphology (Figure 2A-B). Interestingly, homeostatic microglial marker TMEM119 was
298 consistently expressed in our cohort (Figure 2A-D), even though it is known to be
299 downregulated upon microglial activation in various neuropathological conditions[36]. A similar
300 pattern of immunoreactivity is also seen in Matschke et al.[8] and Schwabenland et al.[18].
301 Considering the relatively short hospitalization time prior to death of our COVID-19 cohort
302 (14.5 days), and the similar immunoreactivity pattern compared to other available studies, it
303 could be inferred that TMEM119 downregulation does not occur early in COVID-19.
304 While in both COVID-19 subjects and controls microglial marker TMEM119 and lysosomal-
305 activity marker CD68 were found within the same cell (2A-D), COVID-19 subjects displayed
306 a more widespread CD68+ immunoreactivity (2A-B), with statistically significant differences
307 in CD68 immunoreactive area (A%) at the level of the medulla and midbrain, but not the
308 pons, between the two groups (Figure 2E, Welch ANOVA W= 42.68; medulla $p<0.0001$;
309 pons $p=0.733$; midbrain $p<0.0001$). Ki-67 immunoperoxidase staining, as well as Ki-67 /
310 CD68 double label immunofluorescent staining did not reveal significant Ki-67
311 immunoreactivity ascribable to microglial cells, suggesting local microglial activation and
312 migration without active proliferation in the considered cases. Microglial nodules associated
313 with perineuronal HLA-DR+ / TMEM119+ / CD68+ cells were suggestive of neuronophagia
314 in 18 COVID-19 subjects (Figure 3A-B, 4G, 6F) and were identified at the level of the
315 substantia nigra (N=14), dorsal motor nucleus of the vagus (N=12), medullary reticular
316 formation (N=9), area postrema (N=6) and basal ganglia (N=5); no microglial nodules were
317 found in control cases, regardless of cause of death. Moreover, moderate to severe
318 infiltration of CD68+/TMEM119- cells was found in 23 subjects (2A); given their prominent
319 perivascular localization, these were likely monocyte-derived macrophages.

320

321 *In COVID-19 subjects, a topographically defined pattern of microgliosis was found in the*
322 *medulla oblongata and midbrain.* At the level of the medulla oblongata, Welch one-way

ANOVA of individual counting fields (FOVs) (Figure 4C, F) revealed statistically significant differences ($p<0.001$) in TMEM119+/CD68+ activated microglial cells between the medullary tegmentum (T, FOV-13; 216,84±52,26 microglia / mm^2) and the ventral medulla (pes, P, FOV4-6; 156,09±35,16 microglia / mm^2) (Figure 4E-F); no differences were found between individual counting fields of the same anatomical compartment. Furthermore, no significant differences were found when comparing microglial density between IOT and non-IOT COVID-19 patients, as well as AD and non-AD patients with SARS-CoV-2 infection (Figure 4A). When comparing microglial density between COVID-19 patients and the control cohort, statistically significant differences were found when considering overall medullary microgliosis, as well as single anatomical compartments (Figure 4C).

At the level of the pons, Welch one-way ANOVA of individual counting fields revealed statistically significant differences only between the most dorsally located counting field comprising the locus coeruleus (FOV1), and other counting fields (FOV2-6) (Figure 5D, C). However, as for the medulla, no differences were found between IOT and non-IOT patients, as well as for AD versus non-AD patients (Figure 5A). Differences in overall microgliosis, as well as differences between anatomical compartments, were not significant between COVID-19 subjects and controls (Figure 5B). Hence, while there appears to be a higher degree of microgliosis in proximity to the locus coeruleus in COVID-19 when compared to other regions of the pons, no differences were found within COVID-19 subgroups and when compared to controls, indicating pontine microgliosis as a non-specific alteration in our cohort (Figure 5E-F).

At the level of the midbrain, COVID-19 subjects presented marked topographical differences between counting fields comprising the substantia nigra (midbrain tegmentum, FOV1-2 and FOV3, Figure 6C) when compared to counting fields of the midbrain tectum and pes (FOV4-6), as seen in Figure 6C-D. This anatomically segregated pattern of inflammation targeting mainly the substantia nigra, but also part of the pre-acqueductal tegmentum, indicates an

increasing dorsal-to-ventral gradient of microgliosis which affects the gray matter of the midbrain, sparing counting fields falling within the cerebral peduncle (FOV5-6). Similar to other brainstem levels, no statistically significant differences in overall microgliosis were found when comparing IOT and non-IOT subjects, as well as AD and non-AD subjects (Figure 6A). When compared to controls, COVID-19 subjects presented significantly higher microglial densities when considering both overall microgliosis, as well as microglial densities within anatomical compartments (Figure 6E), suggesting for a COVID-19-specific microglial response at the level of the midbrain (Figure 6F-G).

We also found a strong correlation between microglial densities across the different levels of the brainstem, as well as CD68+ A% of the corresponding level, as summarized in Figure 2G. The strong positive correlation between microglial density and CD68 immunoreactive area further underlines the activated phenotype displayed by microglial cells in COVID-19. Interestingly, in the COVID-19 cohort, hospitalization time was positively correlated to microglial density in the medulla ($r= 0.44$; $p=0.044$), but not with microglial density in the pons and midbrain (Figure 2F). This appears to indicate an increase of microglial densities in the medulla as infection progresses, while the levels of microgliosis within the rest of the brainstem appear to remain relatively stable throughout time. Considering the numerous instances of microglial nodules and neuronophagia encountered in the medulla of the COVID-19 cohort, this is suggestive of prominent medullary impairment ongoing during COVID-19, regardless of oxygenation status or prior neurodegenerative pathology. Conversely, microglial density in the medulla also correlates with hypoxic / ischaemic damage of the brainstem, evaluated along a four-tiered semi-quantitative scale ($r= 0.59$; $p=0.004$), as also seen in Thakur et al.[37]. Hence, while microgliosis is strongly characteristic of COVID-19 subjects and differs from controls, brainstem hypoxia / ischaemia plays a major role in mediating medullary microgliosis, as seen in our cohort and in accordance to previous literature.

SARS-CoV-2 Viral proteins were detected in neurons of the medulla and midbrain in a subset of COVID-19 subjects, *but not in controls.* Immunoperoxidase and immunofluorescent staining for SARS-CoV-2 spike protein and nucleocapsid protein was performed on all samples of included subjects, showing only positive results in cases with SARS-CoV-2 infection, but not in controls, indicating specificity. In particular, viral proteins were detected in seven subjects (#3, #7, #9, #10, #11, #17, #18) within CNS parenchyma and in five subjects (#3, #7, #9, #10, #17) with immunoreactive neurons within the anatomically defined boundaries of the solitary tract nucleus, dorsal motor nucleus of the vagus, nucleus ambiguus and substantia nigra (Figure 7A-D). As seen in double immunofluorescence labeling, SARS-CoV-2 Nucleocapsid protein antibody can be detected in β-III Tubulin (a pan-neuronal marker) immunoreactive structures, such as neuronal somata and neurites in the medulla and midbrain (Figure 7E-H), with no labeling in controls (Figure 7I). At the level of the midbrain, Nucleocapsid protein immunofluorescence was also found within tyrosine hydroxylase immunoreactive neurons and neurites of the substantia nigra, indicating the presence of viral antigens within dopaminergic neurons (Figure 8A-E). Some of these subjects (#7, #9, #11, #17, #18) also displayed endothelial cell immunoreactivity in small vessels of the cerebral cortex (subject #11), deep cerebellar nuclei (#17-18) hippocampus (#7) (Supplementary Figure 2) and midbrain (#9) (Figure 7H); small vessel thromboses, perivascular extravasation and hemorrhagic injury were found within affected regions of these cases.

In case #7, ischaemic injury of the right rostral hippocampal formation due to posterior cerebral artery (PCA) occlusion was associated with perivascular extravasation, edema, fibrinogen leakage and viral protein immunoreactivity within small vessel endothelium, further confirmed by RT-PCR. Acute hemorrhagic injury in the territory of the right middle cerebral artery (MCA) in #11 (Figure 1B) was associated with endothelitis within perilesional

tissue, displaying both viral protein immunoreactive endothelium and positive RT-PCR. Similarly, the deep cerebellar white matter and dentate nuclei in cases #17-18 presented small vessel thromboses and extensive hemorrhagic injury (case #17). Conversely, in some cases with small vessel thromboses within the pons and frontal cortex (e.g. #19-20), viral proteins and RNA was not detectable. There was no correlation between viral protein immunoreactivity / RT-PCR Cycle threshold and hospitalization time (Figure 4E), suggesting no apparent link between the detection of viral antigens and genomic sequences and post-infection interval. However, the actual length of infection, particularly prior to hospitalization, could not always be safely determined, as pre-symptomatic infection could not be excluded, nor evaluated, from the available clinical data. ACE2 receptor protein and TMPRSS2 protein immunoreactivity was compatible with the anatomical distribution of SARS-CoV-2 antigens (Supplementary Figure 1, E-F), as detected with immunoperoxidase staining, but was not consistently replicated in immunofluorescent staining (data not shown). Both proteins were moderately expressed in vascular endothelial cells and brainstem neurons.

RT-PCR analyses of FFPE tissue sections detected viral RNA in COVID-19 cases with viral protein immunoreactivity. Molecular testing by real-time RT-PCR detected SARS-CoV-2 RNA in 10 out of 24 COVID-19 subjects, 9 of whom had also SARS-CoV-2 S and/or N protein-positive IHC / IF (Figure 7L-M, Supplementary Table 2). In positive tissue samples, threshold cycles (Ct) of real-time RT-PCR for SARS-CoV-2 RNA ranged between 33 and 38, while in all samples the Ct values of the internal control RNAseP ranged between 27 and 34. The cycle threshold values for each analyzed section are reported in Supplementary table 2 and in Figure 7L-M for the medulla and midbrain. SARS-CoV-2 subgenomic RNA was investigated but not detected in our specimens, likely due to RNA degradation within FFPE sections, as indicated by the low Ct values of RNAse P.

426 *Viral antigens are associated to higher microglial densities within affected anatomical loci,*
427 *but no differences are found in overall microgliosis, suggesting a specific topographical*
428 *response.* While overall levels of microgliosis within the medulla, pons and midbrain did not
429 differ significantly between COVID-19 subjects with and without detectable viral antigens,
430 Welch one-way ANOVA between anatomical compartments (i.e. tegmentum, tectum and
431 pes) revealed statistically significant differences within the COVID-19 cohort. Indeed,
432 subjects with detectable viral genomic sequences and antigens (RT-PCR+/IHC+) were
433 characterized by higher microglial densities in the medullary (p=0.017) and midbrain
434 tegmentum (p=0.0074) when compared to negative (RT-PCR-/IHC-) COVID-19 subjects, as
435 seen in Figure 4B and 6B. In association with frequent instances of microglial nodules and
436 perineuronal TMEM119+/CD68+ microglial cells suggestive of neuronophagia (Figure 3A-
437 B), this finding suggests a peculiar microglial response towards anatomical loci of the
438 brainstem in which SARS-CoV-2 antigens were detected, even though overall levels of
439 microgliosis within brainstem regions did not appear to differ significantly. Taken together
440 with little-to-no Ki-67 immunoreactivity and no detectable Ki-67+ / CD68+
441 immunofluorescent signal, migration of microglial cells towards the site of injury appears to
442 be the more likely mechanism occurring in COVID-19 inflammation, rather than microglial
443 proliferation within affected regions.

444

445 **Discussion**

446 In the present study, the neuropathological findings of 24 COVID-19 patients were examined
447 and compared with age- and sex-matched controls who died due to pneumonia and / or
448 respiratory insufficiency. Our findings indicate, in line with some of the previous autopsy
449 reports, specific neuropathological alterations in the brains of COVID-19 patients, with
450 particular regard to topographically-defined microgliosis within anatomical loci of the

451 brainstem and viral immunoreactivity in specific CNS compartments, either within the
452 boundaries of brainstem nuclei or in the context of ischaemic and hemorrhagic injuries.
453 Platelet and fibrin microthrombi, in particular, were characteristic findings of the COVID-19
454 cohort, and often affected multiple organs, such as the lungs, liver, intestine, hypopharynx
455 and even the carotid body[10,27-28], as summarized in Table 1. Microthromboses were more
456 frequent within the pons, deep cerebellar nuclei and cerebral cortex. In some cases,
457 hemorrhagic injury and microthromboses were found in regions with viral protein
458 immunoreactivity in vascular endothelial cells.
459 SARS-CoV-2 viral antigens, on the other hand, were confined to specific loci of the CNS. As
460 seen in Figure 7A-H, SARS-CoV-2 appears to be localized preferentially within neurons of
461 the vagal nuclei of the medulla and the substantia nigra, with the exception of one subject
462 who also presented immunoreactive cells throughout the whole brainstem (#3). While
463 Matschke et al.[8] reported SARS-CoV-2 invasion of cranial nerves IX-X, we were unable to
464 replicate these findings within our cohort; furthermore, unlike Meinhardt et al.'s findings[9],
465 viral proteins and RNA were not detectable in any of the sampled olfactory bulbs, tracts and
466 bifurcations, even though moderate edema, moderate-to-severe astrogliosis and moderate
467 microglial activation was encountered in most cases in our study. ACE2 Receptor and
468 TMPRSS-2 protein immunohistochemistry support this topographical localization, with
469 neurons within the dorsal motor nucleus of the vagus, solitary tract nucleus, nucleus
470 Ambiguus and Substantia Nigra being moderately immunoreactive (Supplementary Figure
471 1, E-F).

472 While previous studies identified viral protein immunoreactivity in sparse cells throughout
473 the brainstem[8-18] without specific topography, our findings appear to be in line with available
474 animal studies on other coronaviruses, i.e. SARS-CoV and MERS-CoV, which are known to
475 be able to infect the brainstem, and particularly the dorsal motor nucleus of the vagus,
476 solitary tract nucleus and nucleus ambiguus, so that an analog pattern of neuroinvasion for

SARS-CoV-2 has been suggested[17,29-31]. The peculiar and unexpected finding in our cohort was the detection of viral antigens and genomic sequences within the substantia nigra, not matching any known models of coronavirus neurotropism. Interestingly, SARS-CoV-2 S and N protein were detected in both tyrosine hydroxylase positive and negative neurons (Figure 8). Immunoreactive neurons of the substantia nigra were frequently found in proximity to blood vessels, which were at times immunoreactive to viral proteins as well (Figure 7H, Supplementary Figure 2). Hence, aside from olfactory-transmucosal transmission identified by Meinhardt et al.[9], and vagus/glossopharyngeal-mediated invasion identified by Matshke et al.[8], SARS-CoV-2 may gain access to other districts of the CNS either through a yet-unknown neuronal route or, as suggested by our findings in the midbrain and as seen in Schwabeland et al.'s study[18], by crossing the blood-brain-barrier and infecting structures of the peri- and juxtavascular compartment. We believe these findings encourage further research on the possibility that these events may be the trigger of a neurodegenerative process such as Parkinson disease in susceptible individuals. Future studies on COVID-19 survivors and Long COVID patients are therefore warranted[39].

However, despite the detection of viral proteins and genomic sequences in restricted regions of the brainstem, we found no evident neuropathological alterations in SARS-CoV-2 infected cells, such as necrotic changes and other cytological alterations, that could hint towards possible direct consequences of viral invasion in human neurons. COVID-19 is characterized by different evolutionary phases and heterogeneous individual responses, and the short interval between infection and death in our cohort (mean hospitalization time = 14 days), as well as the fact that included patients died during the acute phase of the disease, may not be sufficient to determine detectable neuropathological alterations in affected cells as a direct consequence of viral invasion, which may require more time to develop[3,31]. Lastly, the detection of viral proteins in a subset of patients (5 out of 24), as

seen in this and previous studies may be related to the particularly severe disease, and concurring comorbidities, of the patients subject to neuropathological examination.

Hence, while the consequences of SARS-CoV-2 neurotropism in the medulla have been widely discussed in literature, and are supported by the detection of viral proteins and genomic sequences in our study, the absence of direct neuronal damage and the impossibility of performing functional assays on post-mortem samples should be taken into consideration when discussing the clinical implications of COVID-19 neuropathology. Future studies on "long COVID" patients[3] may be able to shed a light on the long-term consequences of COVID-19, particularly concerning the detection of SARS-CoV-2 within the CNS after the acute phase of the disease, and whether or not this leads to specific neuropathological alterations as a consequence of viral invasion.

Concerning microglial activation and density, our findings appear to be in line with Schwabenland et al.[18], who identified microglial nodules and parenchymal reactive microglia as hallmark for COVID-19, in contrast to both controls and ExtraCorporeal Membrane Oxygenation (ECMO) patients. In our cohort, patients with pneumonia and / or respiratory failure served as control group and, although also characterized by microglial activation, displayed lower microglial counts in the medulla and midbrain, but not in the pons, when compared to COVID-19 subjects. We also found no significant effect of oxygen therapy on microglial density within the COVID-19 group. Conversely, Deigendesh et al.[33] found significant differences in HLA-DR+ activated microglia when comparing COVID-19 subjects to non-septic controls, but no differences were found with patients who had died under septic conditions; according to the authors[33] this may represent a histopathological correlate of critical illness-related encephalopathy, rather than a COVID-19-specific finding. Aside from the distinct populations serving as control subjects, significant methodological differences between these studies must be taken into consideration. Our approach to microglial

quantification was more similar to Schwabenland et al.[18], as digitally-assisted manual counting of TMEM119+ cells, a homeostatic microglia-specific marker, was performed to estimate microgliosis; however, we also expanded on these findings by estimating microgliosis in a topographically dependent manner by employing set counting fields within anatomically defined regions; conversely Deigendesh et al.[33] quantified HLA-DR immunoreactive area, a marker expressed on both microglia and on infiltrating lympho-monocytic cells, as a fraction of the counting field (A%), and not as individual particles. Hence, while our estimation selectively reflects the activity of microglial cells in COVID-19 and pneumonia controls within anatomically defined regions of the brainstem, Deigendesh's study offers a broader representation of overall brainstem inflammation under different conditions, including patients deceased under septic conditions, explaining differences between our studies.

Interestingly, while no evidence of direct neuronal damage was found in SARS-CoV-2 infected cells, microglial densities within affected anatomical loci differed between subjects with and without detectable viral antigens and genomic sequences (RT-PCR/IHC+ versus RT-PCR/IHC- in Figure 4B and 6B), suggesting a link between the detection of SARS-CoV-2 antigens and microglial response. Conversely, overall microglial density (i.e. without topographical delineation) did not differ between the two groups, and a strong correlation between microgliosis and hypoxic / ischaemic damage at the level of the brainstem was found. Hence, while we found a suggestive link between microgliosis and the detection of SARS-CoV-2 antigens in our cohort, other factors such as hypoxia / ischaemia and systemic inflammation / cytokine storm ongoing during COVID-19, as previously reported by Thakur et al[37], are likely to play a more prominent role in determining brainstem microgliosis, in accordance to previous studies[33].

Conclusions

The present study contributes to define the spectrum of neuropathological alterations in COVID-19, as well as the neuroinvasive potential of SARS-CoV-2 within the CNS. Unlike previous findings, we have documented a subset of COVID-19 cases in which viral proteins and genomic sequences were detectable within anatomically defined regions of the CNS. Similarly, microglial activation in the brainstem appears to differ between COVID-19 and pneumonia / respiratory failure controls, with the former also presenting a pattern of increased microglial density in specific compartments of the medulla and midbrain. However, despite this evidence supporting the neuroinvasive potential of SARS-CoV-2, neuropathological alterations encountered in our cohort cannot be ascribed to viral antigens detected in the brainstem. In line with other studies in literature, hypoxic / ischaemic damage and systemic inflammation likely represent major contributors in determining neuropathological alterations in COVID-19, with little-to-no evidence indicating direct viral damage of the central nervous system in humans. Moreover, further investigation is required to determine whether or not SARS-CoV-2 neurotropism represents a major component of COVID-19 in the general population, as subjects included in neuropathological studies often present a much more severe course of the disease and major medical comorbidities. Nevertheless, the findings of our study suggest the possibility that, although not frequently, SARS-CoV-2 may gain access to specific regions of the central nervous system, especially the vagal nuclei of the medulla and the substantia nigra in the midbrain. As direct neuropathological alterations determined by SARS-CoV-2 neurotropism may not be detectable in subjects deceased during the acute phase of the disease, future studies are required to determine whether or not SARS-CoV-2 neurotropism is present in chronic COVID-19 patients, or in COVID-19 survivors suffering from the long-term effects of infection, and if eventual neuropathological alterations in these subjects can be ascribed to viral tropism, rather than immune-mediated mechanisms.

Limitations of the study

This study is based on post-mortem tissue samples obtained during the first wave of the COVID-19 pandemic in Italy. While the neuropathological alterations encountered in our work contribute to define the pathological mechanisms of COVID-19 and SARS-CoV-2 infection in the CNS, the lack of exhaustive post-infection neurological evaluation of included patients does not allow for unequivocal clinico-pathological correlations. It must also be considered that most patients included in the study died during the peak of the sanitary emergency in Italy, one of the first countries to face the COVID-19 pandemic in Europe, and neurological evaluation was not always possible. Hence, it remains to be determined whether the neuropathological alterations observed in this study are also linked to neurological symptoms, and whether they are also present in COVID-19 survivors.

Unlike previous studies in literature, we have included 18 controls who died due to pneumonia, respiratory insufficiency or multiorgan failure, rather than healthy controls. Retrospective selection of control subjects, however, could lead to unwanted selection bias. Furthermore, from the available clinical data of our controls, we have found no instances of intensive oxygen therapy or mechanical ventilation, but incompleteness of available clinical records cannot entirely be excluded. For this purpose, we have also performed comparisons within the COVID-19 group, identifying no statistically significant differences between subjects with and without neurodegenerative conditions, and no influence of oxygen therapy on brainstem microgliosis. The involvement of other brain regions, such the cerebral and cerebellar cortex and the basal ganglia, cannot be excluded but is beyond the scopes of this study. Moreover, as all patients died during the first wave of the COVID-19 pandemic, our findings may not reflect the possible neuropathological alterations encountered in patients affected by SARS-CoV-2 variants.

603 Limitations to viral antigen / RNA detection in our study must also be considered. Real-time
604 RT-PCR cannot exclude detection of viral RNA in blood vessels within samples. While
605 particular care was taken to avoid contamination by employing sterile instruments and
606 disposable microtome blades when sampling FFPE sections for RT-PCR analyses, the main
607 strength of our study was the complementary use of immunoperoxidase and
608 immunofluorescent staining with different antibodies to detect viral antigen as an indicator
609 of viral tropism. This is further strengthened by the strong concordance between these
610 assays in our cohort, quantified by a statistically significant positive correlation between RT-
611 PCR cycle threshold and IHC positivity ($r=0.87$, $p<0.0001$).

612 In conclusion, further investigation is required to determine the direct effects of viral invasion
613 within the CNS, with particular regard to cases of long-lasting infection and in COVID-19
614 survivors.

615

616 **Acknowledgements**

617 We are grateful to Prof. James E. Goldman for his feedback and suggestions concerning
618 our study.

619

620 **Data Sharing:** data is available from the corresponding author upon request; raw data
621 underlying graphs and statistical analyses has been provided to the editor, reviewers, and
622 is available upon reasonable request.

623 **Conflicts of interest:** the authors declare no conflicts of interest.

624 **Ethical approval:** All procedures were carried out in accordance to the Declaration of
625 Helsinki. Samples were anonymous to the investigators and used in accordance with the

626 directives of the Committee of the Ministers of EU member states on the use of samples of
627 human origin for research.

Figure Legends

Figure 1. A) Study Workflow. Brain sections of multiple sites were sampled from 24 COVID-19 patients and 18 age- and sex-matched controls who died due to pneumonia and / or respiratory failure. **B)** Left, coronal brain section of Subject #11 revealing extensive hemorrhagic injury in the territory of the middle cerebral artery. Right, sampling procedure of the brainstem through axial sections passing perpendicularly to the floor of the fourth ventricle. **C)** Haematoxylin and eosin photomicrographs of the Dorsal Motor Nucleus of the Vagus in the medulla oblongata displaying various degrees of hypoxic / ischaemic damage in COVID-19 subjects (upper row) and controls (lower row) **D)** Platelet microthrombi at the level of the pons and cerebral cortex, CD61 immunohistochemistry.

Figure 2. Double label TMEM119 (microglia marker, red) / CD68 (lysosomal activity marker, green) fluorescent immunohistochemistry in COVID-19 and control subjects. **A-B)** in COVID-19, microglial cells present a distinctly activated phenotype whilst maintaining homeostatic microglial marker TMEM119 (Red) and displaying increased lysosomal activity (CD68, green). Arrows indicate CD68+ / TMEM119- monocyte/macrophage in the parenchyma. **C-D)** In control subjects, TMEM119 marks both the soma and sparse ramifications of resident microglia, suggesting less prominent activation without significant marker downregulation. CD68 immunoreactivity (green) is also present, but not as distributed as in COVID-19. **E)** Welch one-way ANOVA of CD68+ A% in COVID-19 and controls reveals statistically significant differences between the two groups at the level of the medulla ($p<0.0001$) and midbrain ($p<0.0001$), but not the pons. **F)** Spearman correlation between microglial densities across brainstem levels and hospitalization time reveals a statistically significant positive correlation between medullary microgliosis and hospitalization time ($r= 0.44$; $p=0.044$). **G)** Correlation matrix between microglial densities and CD68+ A% across brainstem levels.

Figure 3. A) Low-magnification perspective of the medulla oblongata in COVID-19, displaying a ventral-to-dorsal increasing gradient of microglial densities (TMEM119, red; Beta-III Tubulin, green) **B-C)** Double label TMEM119 (microglial marker, red) and Beta-III Tubulin (neuronal marker, green) immunofluorescent staining at the level of the medulla oblongata. Insets display neuronophagia at the level of the dorsal motor nucleus of the vagus in two COVID-19 subjects.

Figure 4. A) Welch corrected T-test plot of microglial densities (microglia / mm^2) in the medulla oblongata of COVID-19 subjects treated (n=10, red) and not treated (n=11, black) with intensive oxygen therapy ($p>0.05$), and of COVID-19 subjects with (n=5, red) and without (n=16, black) Alzheimer's Disease neuropathological changes ($p>0.05$). **B)** Welch one-way ANOVA between anatomical compartments (T, tegmentum; P, pes) between COVID-19 subjects with (n=5, red) and without (n=16) viral tropism (RT-PCR/IHC+ versus RT-PCR/IHC-) reveals statistically significant differences at the level of the medullary tegmentum ($p=0.017$). **C)** Welch one-way ANOVA between anatomical compartments (T, tegmentum; P, pes) between COVID-19 subjects (n=21, red) and controls (n=18, black) reveals statistically significant differences both at the level of the medullary tegmentum ($p<0.0001$) and pes ($p=0.017$). **D)** Welch one-way ANOVA of microglial densities per

counting fields (FOV) reveals statistically significant differences between FOVs of the Tegmentum (T; FOV1-3) when compared to FOVs of the Pes (P; FOV4-6). **E)** Correlation heatmap between COVID-19 subject clinical data and neuropathological findings. **F)** Anatomical heatmap of activated microglia within the medulla oblongata in COVID-19. **G-H)** TMEM119 immunoperoxidase staining of comparable regions of the medulla oblongata in COVID-19 subjects (above) and controls (below). Inset: neuronophagia in the dorsal motor nucleus of the vagus. Arrow: microglial nodule.

Figure 5. A) Welch corrected T-test plot of microglial densities (microglia / mm^2) in the pons of COVID-19 subjects with (n=5, red) and without (n=16, black) Alzheimer's Disease neuropathological changes ($p>0.05$), and of COVID-19 subjects treated (n=10, red) and not treated (n=13, black) with intensive oxygen therapy ($p>0.05$). **B)** Welch one-way ANOVA between anatomical compartments (T, tegmentum; P, pes) between COVID-19 subjects (n=23, red) and controls (n=18, black) reveals no statistically significant differences either at the level of the medullary tegmentum ($p=0.55$) and pes ($p=0.98$). **C)** Anatomical heatmap of activated microglia within the pons in COVID-19. **D)** Welch one-way ANOVA of microglial densities per counting fields (FOV) reveals statistically significant differences between FOV1 (dorsal pons, including locus coeruleus) with other pontine counting fields. **E-F)** TMEM119 immunoperoxidase staining of comparable regions of the pons in COVID-19 subjects (above) and controls (below).

Figure 6. A) Welch corrected T-test plot of microglial densities (microglia / mm^2) in the midbrain of COVID-19 subjects with (n=5, red) and without (n=16, black) Alzheimer's Disease neuropathological changes ($p>0.05$), and of COVID-19 subjects treated (n=10, red) and not treated (n=11, black) with intensive oxygen therapy ($p>0.05$). **B)** Welch one-way ANOVA between anatomical compartments (TG, tegmentum; TC, tectum; P, pes) between COVID-19 subjects with (n=5, red) and without (n=18) viral tropism (RT-PCR/IHC+ versus RT-PCR/IHC-) reveals statistically significant differences at the level of the midbrain tegmentum ($p=0.0074$), but not other anatomical districts. **C)** Anatomical heatmap of activated microglia within the medulla oblongata in COVID-19. **D)** Welch one-way ANOVA of microglial densities per counting fields (FOV) reveals statistically significant differences between FOVs of the Tegmentum (T; FOV1-2) when compared to FOVs of the Pes (P; FOV5-6), suggesting for a localized pattern of microgliosis comprising the preacqueductal tegmentum and the substantia nigra. **E)** Welch one-way ANOVA between anatomical compartments (TG, tegmentum; TC, tectum; P, pes) between COVID-19 subjects (n=23, red) and controls (n=18, black) reveals statistically significant differences between all anatomical districts of the midbrain ($p<0.0001$). **F-G)** TMEM119 immunoperoxidase staining of comparable regions of the midbrain in COVID-19 subjects (above) and controls (below). Inset: perineuronal microglia in the substantia nigra. COVID-19 subjects often present distinct microglial nodules.

Figure 7. Topographical localization of SARS-CoV-2 Viral Protein Immunoreactivities (Triangles, Right Half) and Microglial Nodules (Asterisks, Left Half) throughout the brainstem. **A)** At the level of the Mesencephalon, Immunoreactivities are found mainly within the boundaries of the substantia nigra, with the exception of Subject #3, which also presented immunoreactive neurons within the Interstitial Nucleus of Cajal; Microglial

nodules were confined mainly within the boundaries of the tegmentum, and were not detected neither within the pes nor the tectum. **A1)** SARS-CoV-2 Spike Protein IHC at the level of the Substantia Nigra reveals immunoreactive neurons (mean of 2 immunoreactivities per mm^2) with well-marked processes (black arrows); negative neurons can also be found nearby (white arrows). **A2)** SARS-CoV-2 Nucleocapsid Protein IHC reveals a similar pattern of immunoreactive neurons and axons throughout the substantia nigra. **B)** At the level of the pons, Subject #3 presented immunoreactive neurons (mean of 5 immunoreactivities per mm^2) within the basilary nuclei, while microglial nodules were found both within the basis, as well as the dorsal pons in proximity to the facial nucleus. **B1)** SARS-CoV-2 Spike Protein IHC at the level of the pons in Subject #3, displaying immunoreactive neurons (black arrows) within the basilary nuclei of the pons; non-reactive cells can also be appreciated (white arrows) **C)** At the level of the upper medulla oblongata, immunoreactivities were found at the level of the dorsal motor nucleus of the vagus, solitary tract nucleus and nucleus ambiguus; microglial nodules were prominent within the Vagal Trigone and Area Postrema, but were also found within the reticular formation and the inferior olivary complex. **C1-2)** SARS-CoV-2 Spike Protein IHC at the level of the solitary tract nucleus and nucleus ambiguus; immunoreactive neurons can be seen within the anatomical boundaries of these nuclei (black arrows), along with non-reactive cells (white arrows). Inset of a single reactive neuron within the solitary tract nucleus, Spike Protein immunohistochemistry. **D)** At the level of the Lower Medulla Oblongata, Immunoreactivities were found at the level of the spinal trigeminal nucleus and medullary reticular formation. Microglial nodules were found within the medullary reticular formation. **D1)** SARS-CoV-2 Spike Protein IHC at the level of the medullary reticular formation in the lower medulla (black arrows); non-reactive cells are indicated with a white arrow. **E-I)** Double label N and S Protein (red) and Beta-III Tubulin (green) fluorescent immunohistochemistry in COVID-19 subjects (E-H) and controls (I). Distinct immunoreactive neurons and neurites can be appreciated in both the medulla (dorsal motor nucleus of the vagus) and midbrain (substantia nigra) (E-G). Juxtavascular immunoreactive neurons in proximity to an immunoreactive vessel in the midbrain of COVID-19 subject #9 (H, inset). Control subjects present no viral protein immunoreactivity (I). **L-M)** N and S protein IHC, real time RT-PCR Cycle Thresholds for SARS-CoV-2 N Gene and RNAseP quality control in our COVID-19 cohort at the level of the medulla (L) and midbrain (M).

Figure 8. Double label N Protein (red) and Tyrosine Hydroxylase (green) fluorescent immunohistochemistry at the level of the substantia nigra in the midbrain. **A-C)** in COVID-19, Both TH+ and TH- neurons display N protein immunoreactivity. **D-E)** in COVID-19 subjects with negative RT-PCR/IHC (D) as well as non-COVID controls (E) no N protein staining was detected.

REFERENCES

1. Ellul, M.A., Benjamin, L., Singh, B., et al. Neurological associations of COVID-19. Lancet Neurol. **19,** 767–783 (2020) doi:10.1016/s1474-4422(20)30221-0.
2. Helms, J., Kremer, S., Merdji, H., et al. Neurologic Features in Severe SARS-CoV-2 Infection. N. Engl. J. Med. **382**, 2268–2270 (2020) doi:10.1056/nejmc2008597.
3. Huang, C., Huang, L., Wang, Y., et al. 6-month consequences of COVID-19 in paients discharged from hospital: a cohort study. Lancet **397**, 220-232 (2021)
4. Iadecola, C., Anrather, J., Kamel, H. Effects of COVID-19 on the Nervous System. Cell **183**, 16–27 (2020) doi:10.1016/j.cell.2020.08.028.
5. Mao, L., Jin, H., Wang, M., et al. Neurologic Manifestations of Hospitalized Patients with Coronavirus Disease 2019 in Wuhan, China. JAMA Neurol. **77**, 683 (2020) doi:10.1001/jamaneurol.2020.1127.
6. Puelles, V.G., Lütgehetmann, M., Lindenmeyer, M.T., et al. Multiorgan and Renal Tropism of SARS-CoV-2. N. Engl. J. Med. **383**, 590–592 (2020) doi:10.1056/nejmc2011400.
7. Jacob, F., Pather, S.R., Huang, W.K., Zhang, F., et al. Human Pluripotent Stem Cell-Derived Neural Cells and Brain Organoids Reveal SARS-CoV-2 Neurotropism Predominates in Choroid Plexus Epithelium. Cell Stem Cell. **27**, 937-950. (2020) doi: 10.1016/j.stem.2020.09.016.
8. Matschke, J., Lütgehetmann, M., Hagel, C., et al. Neuropathology of patients with COVID-19 in Germany: a post-mortem case series. Lancet Neurol. **19**, 919-929 (2020) doi: 10.1016/S1474-4422(20)30308-2.
9. Meinhardt, J., Radke, J., Dittmayer, C., et al. Olfactory transmucosal SARS-CoV-2 invasion as a port of central nervous system entry in individuals with COVID-19. Nat Neurosci. **24**, 168-175 (2021) doi: 10.1038/s41593-020-00758-5.
10. Porzionato, A., Emmi, A., Contran, M., et al. The Carotid Body in COVID-19: histopathological and virological analyses of an autopsy case series. Front. Immunn. (2021) doi:10.3389/fimmu.2021.736529
11. Solomon, I.H., Normandin, E., Bhattacharyya, S., et al. Neuropathological Features of Covid-19. N Engl J Med. **383**, 989-992 (2020) doi: 10.1056/NEJMc2019373.
12. Trevisan, M., Riccetti, S., Sinigaglia, A., Barzon, L. SARS-CoV-2 Infection and Disease Modelling Using Stem Cell Technology and Organoids. Int J Mol Sci. **22**, 2356 (2021)
13. Bauer, L., Lendemeijer, B., Leijten, L., et al. Replication Kinetics, Cell Tropism, and Associated Immune Responses in SARS-CoV-2- and H5N1 Virus-Infected Human Induced Pluripotent Stem Cell-Derived Neural Models. mSphere 6:e0027021, (2021) doi: 10.1128/mSphere.00270-21.
14. Pellegrini, L., Albecka, A., Mallery, D.L., Kellner, M.J., Paul, D., Carter, A.P., James, L.C., Lancaster, M.A. SARS-CoV-2 Infects the Brain Choroid Plexus and Disrupts the Blood-CSF Barrier in Human Brain Organoids. Cell Stem Cell. **27**, 951-961.e5. (2020) doi: 10.1016/j.stem.2020.10.001.
15. Song, E., Zhang, C., Israelow, B., Lu-Culligan, A., Prado, A.V., Skriabine, S., Lu, P., et al. Neuroinvasion of SARS-CoV-2 in human and mouse brain. J Exp Med. 218:e20202135. (2021) doi: 10.1084/jem.20202135.
16. Zheng, J., Wong, L.R., Li, K., et al. COVID-19 treatments and pathogenesis including anosmia in K18-hACE2 mice. Nature **589**, 603-607 (2021) doi: 10.1038/s41586-020-2943-z.

17. Desforges, M., Le Coupanec, A., Stodola, J.K., Meessen-Pinard, M., Talbot, P.J. Human coronaviruses: viral and cellular factors involved in neuroinvasiveness and neuropathogenesis. Virus Res. **194**, 145-58 (2014) doi: 10.1016/j.virusres.2014.09.011.
18. Schwabenland, M., Salié, H., Tanevski, J., et al. Deep spatial profiling of human COVID-19 brains reveals neuroinflammation with distinct microanatomical microglia-T-cell interactions. Immunity **54**, 1594-1610.e11. (2021) doi: 10.1016/j.immuni.2021.06.002.
19. Lee, M.H., Perl, D.P,, Nair, G., et al. Microvascular Injury in the Brains of Patients with Covid-19. N Engl J Med. **384**, 481-483. (2021) doi: 10.1056/NEJMc2033369.
20. Yang, A.C., Kern, F., Losada, P.M., et al. Dysregulation of brain and choroid plexus cell types in severe COVID-19. Nature **595**, 565-571 (2021) doi: 10.1038/s41586-021-03710-0.
21. Schurink, B., Roos, E., Radonic, T., et al. Viral presence and immunopathology in patients with lethal COVID-19: a prospective autopsy cohort. Lancet Microbe **1**, e290-e299 (2020)
22. Barton, L.M., Duval, E.J., Stroberg, E., Ghosh, S., Mukhopadhyay, S. COVID-19 Autopsies, Oklahoma, USA. Am J Clin Pathol **153**, 725-733 (2020) doi: 10.1093/ajcp/aqaa062.
23. Reichard, R.R., Kashani, K.B., Boire, N.A., Constantopoulos, E., Guo, Y., Lucchinetti, C.F. Neuropathology of COVID-19: a spectrum of vascular and acute disseminated encephalomyelitis (ADEM)-like pathology. Acta Neuropathol. **140**, 1-6 (2020) doi: 10.1007/s00401-020-02166-2.
24. Schaller, T., Hirschbühl, K., Burkhardt, K. Postmortem Examination of Patients With COVID-19. JAMA **323**, 2518-2520 (2020) doi: 10.1001/jama.2020.8907.
25. Lavezzo, E., Franchin, E., Ciavarella, C., Cuomo-Dannenburg, G., Barzon, L., et al. Suppression of a SARS-CoV-2 outbreak in the Italian municipality of Vo'. Nature. **584**, 425-429 (2020) doi: 10.1038/s41586-020-2488-1.
26. Mai, J. K., and Paxinos, G. *The Human Nervous System,* 3rd Edn. (Elsevier, Amsterdam, 2012)
27. Basso, C., Leone, O., Rizzo, S., et al. Pathological features of COVID-19-associated myocardial injury: a multicentre cardiovascular pathology study. Eur Heart J. **41**, 3827-3835 (2021) doi: 10.1093/eurheartj/ehaa664.
28. Porzionato, A., Stocco, E., Emmi, A., et al. Hypopharyngeal Ulcers in COVID-19: Histopathological and Virological Analyses - A Case Report. Front Immunol. **12**, e676828. (2021) doi: 10.3389/fimmu.2021.676828.
29. Li, Y.C., Bai, W.Z., Hashikawa, T. The neuroinvasive potential of SARS-CoV2 may play a role in the respiratory failure of COVID-19 patients. J Med Virol. **92**, 552-555. (2020) doi: 10.1002/jmv.25728.
30. Porzionato, A., Emmi, A., Barbon, S., Boscolo-Berto, R., Stecco, C., Stocco, E., Macchi, V., De Caro, R. Sympathetic activation: a potential link between comorbidities and COVID-19. FEBS J. **287**, 3681-3688 (2020) doi: 10.1111/febs.15481.
31. Porzionato, A., Emmi, A., Stocco, E., Barbon, S., Boscolo-Berto, R., Macchi, V., De Caro, R. The potential role of the carotid body in COVID-19. Am J Physiol Lung Cell Mol Physiol. **319**, 620-626. (2020) doi: 10.1152/ajplung.00309.2020.
32. Iturriaga, R., Castillo-Galán, S. Potential contribution of carotid body-induced sympathetic and renin-angiotensin system overflow to pulmonary hypertension in intermittent hypoxia. Curr Hypertens Rep. **21**, 89 (2019)

33. Deigendesch, N., Sironi, L., Kutza, M., et al. Correlates of critical illness-related encephalopathy predominate postmortem COVID-19 neuropathology. Acta Neuropathol. **140**, 583-586 (2020) doi: 10.1007/s00401-020-02213-y.
34. Emmi, A., Antonini, A., Macchi, V., Porzionato, A., De Caro, R. Anatomy and Connectivity of the Subthalamic Nucleus in Humans and Non-human Primates. Front Neuroanat. **14**, 13 (2020) doi: 10.3389/fnana.2020.00013.
35. Emmi, A., Porzionato, A., Contran, M., De Rose, E., Macchi, V., De Caro, R. 3D Reconstruction of the Morpho-Functional Topography of the Human Vagal Trigone. Front Neuroanat. **15**, 663399(2021) doi: 10.3389/fnana.2021.663399.
36. Schwabenland, M., Brück, W., Priller, J., Stadelmann, C., Lassmann, H., Prinz, M. Analyzing microglial phenotypes across neuropathologies: a practical guide. Acta Neuropathol. **142**, 923-936. (2021) doi: 10.1007/s00401-021-02370-8.
37. Thakur, K.T., Miller, E.H., Glendinning, M.D., et al. COVID-19 neuropathology at Columbia University Irving Medical Center/New York Presbyterian Hospital. Brain. **144**, 2696-2708 (2021) doi: 10.1093/brain/awab148.
38. Fullard, J.F., Lee, H.C., Voloudakis, G., et al. Single-nucleus transcriptome analysis of human brain immune response in patients with severe COVID-19. Genome Med. **13**, 118 (2021) 19. doi:10.1186/s13073-021-00933-8
39. Sulzer, D., Antonini, A., Leta, V., Nordvig, A., Smeyne, R. J., Goldman, J. E., et al. COVID-19 and possible links with Parkinson's disease and parkinsonism: from bench to bedside. NPJ Parkinson's disease, **6**, 18 (2020) https://doi.org/10.1038/s41531-020-00123-0

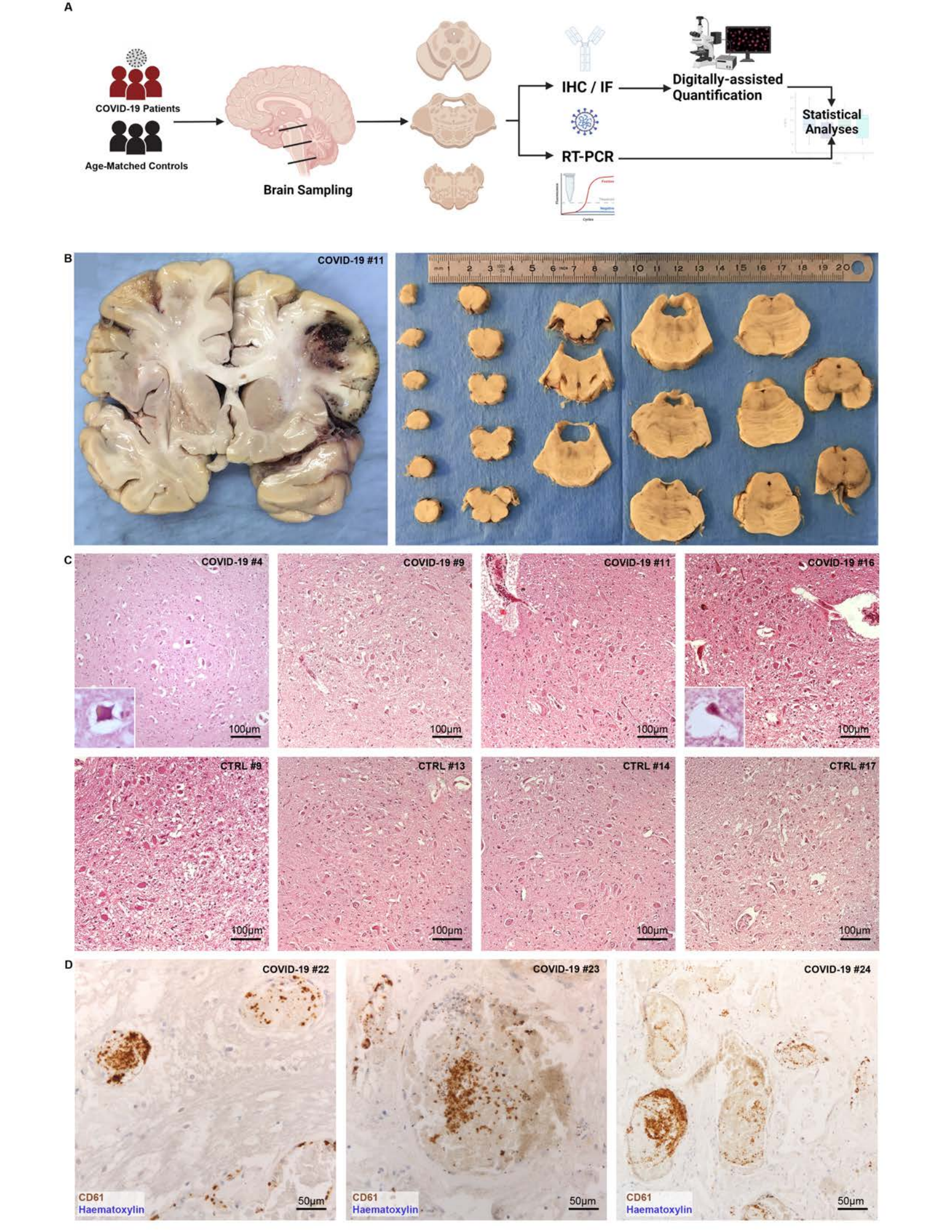
A
COVID-19 Patients
Age-Matched Controls
Brain Sampling
IHC / IF
RT-PCR
Digitally-assisted Quantification
Statistical Analyses
B
COVID-19 #11
C
COVID-19 #4
COVID-19 #9
COVID-19 #11
COVID-19 #16
CTRL #9
CTRL #13
CTRL #14
CTRL #17
100µm
D
COVID-19 #22
COVID-19 #23
COVID-19 #24
CD61
Haematoxylin
50µm

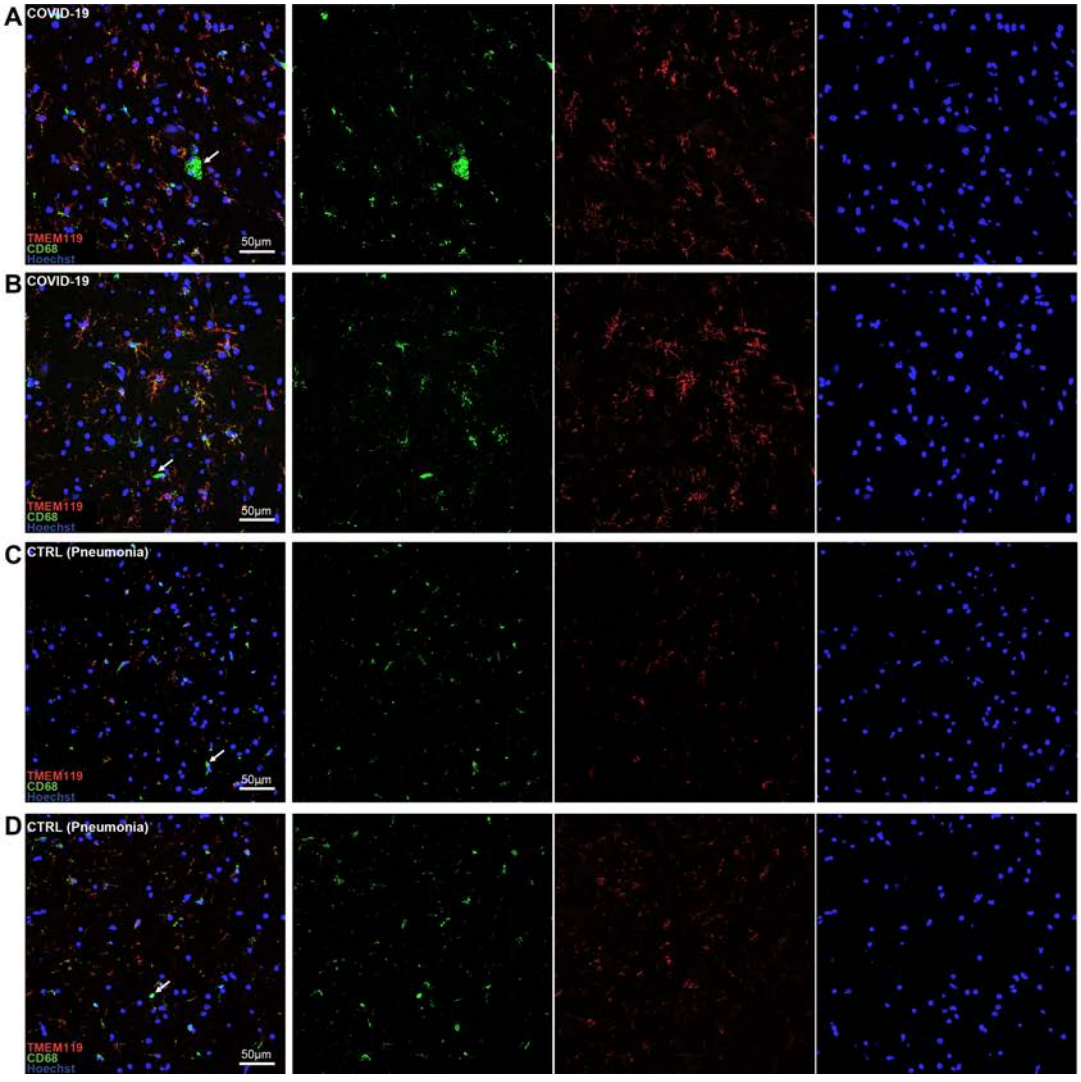
A
COVID-19
TMEM119
CD68
Hoechst
50μm
B
COVID-19
TMEM119
CD68
Hoechst
50μm
C
CTRL (Pneumonia)
TMEM119
CD68
Hoechst
50μm
D
CTRL (Pneumonia)
TMEM119
CD68
Hoechst
50μm

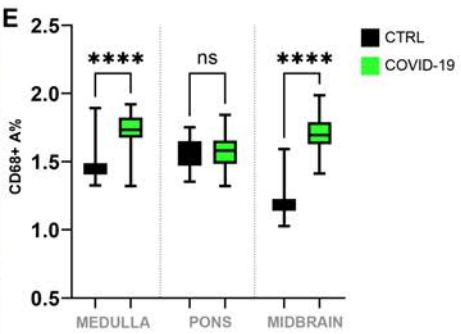
E
CTRL
COVID-19
****
ns
****
CD68+ A%
2.5
2.0
1.5
1.0
0.5
MEDULLA
PONS
MIDBRAIN

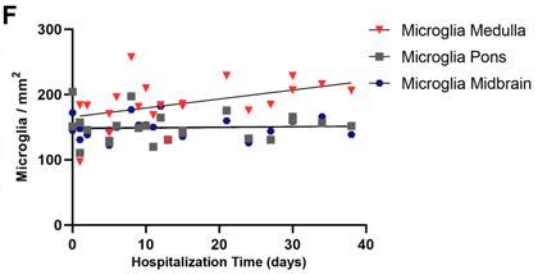
F
Microglia Medulla
Microglia Pons
Microglia Midbrain
Microglia / mm²
300
200
100
0
0
10
20
30
40
Hospitalization Time (days)

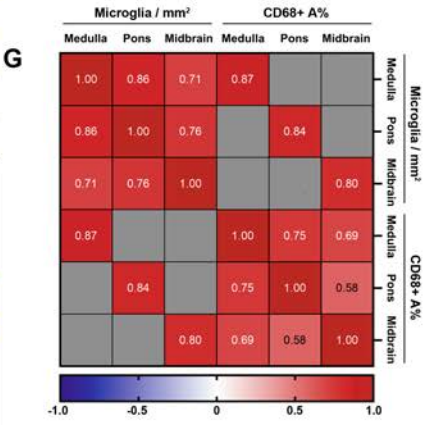
G
Microglia / mm²
CD68+ A%
Medulla
Pons
Midbrain
Medulla
Pons
Midbrain
1.00 0.86 0.71 0.87
0.86 1.00 0.76 0.84
0.71 0.76 1.00 0.80
0.87 1.00 0.75 0.69
0.84 0.75 1.00 0.58
0.80 0.69 0.58 1.00
Microglia / mm²
CD68+ A%
-1.0
-0.5
0
0.5
1.0

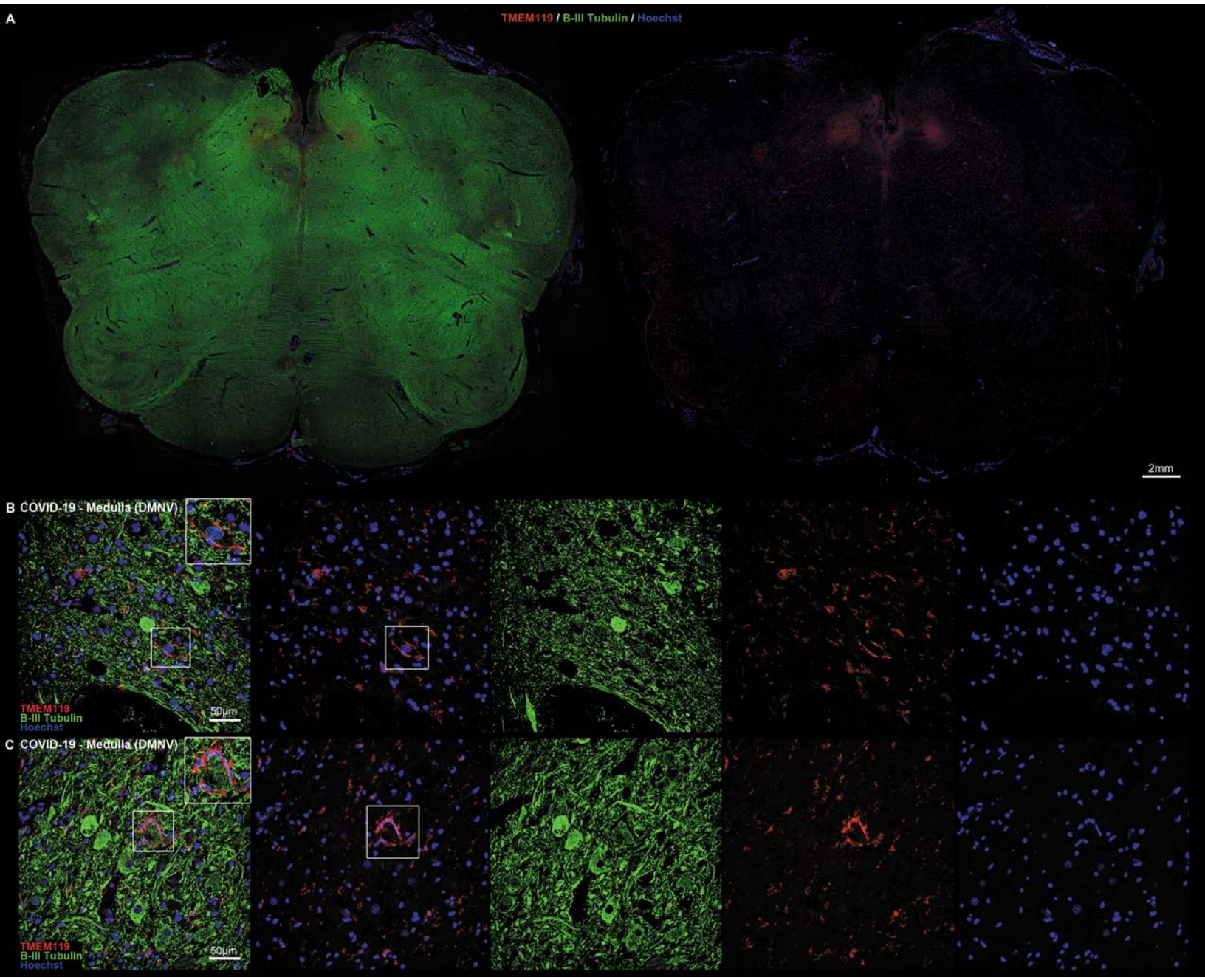
A
TMEM119 / B-III Tubulin / Hoechst
2mm
B COVID-19 - Medulla (DMNV)
TMEM119
B-III Tubulin
Hoechst
50µm
C COVID-19 - Medulla (DMNV)
TMEM119
B-III Tubulin
Hoechst
50µm

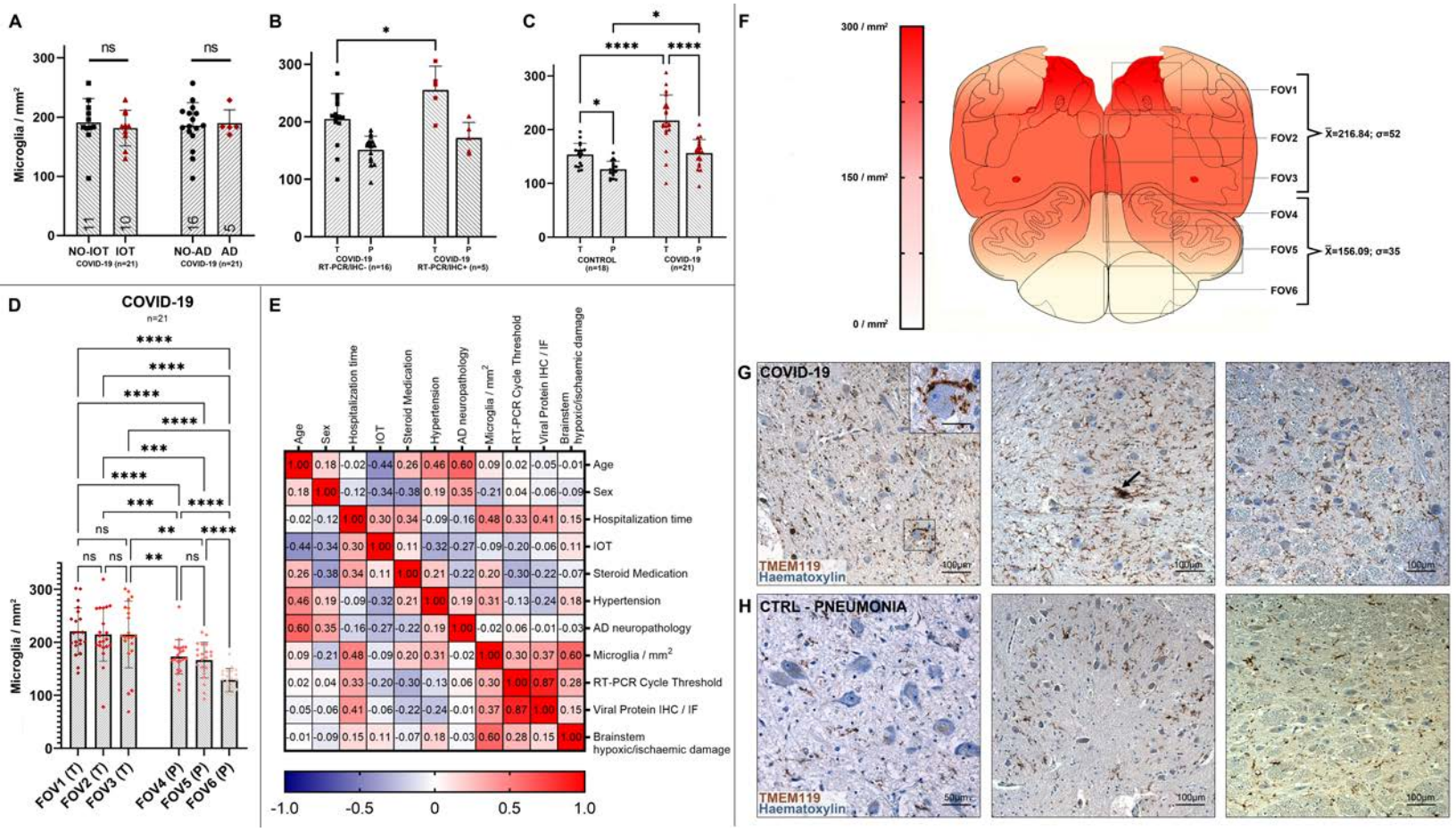
A
Microglia / mm²
ns
ns
NO-IOT
IOT
NO-AD
AD
COVID-19 (n=21)
B
*
T
P
COVID-19 RT-PCR/IHC- (n=16)
COVID-19 RT-PCR/IHC+ (n=5)
C
*
****
CONTROL (n=18)
COVID-19 (n=21)
D
COVID-19
n=21
FOV1 (T)
FOV2 (T)
FOV3 (T)
FOV4 (P)
FOV5 (P)
FOV6 (P)
E
Age
Sex
Hospitalization time
IOT
Steroid Medication
Hypertension
AD neuropathology
Microglia / mm²
RT-PCR Cycle Threshold
Viral Protein IHC / IF
Brainstem hypoxic/ischaemic damage
F
300 / mm²
150 / mm²
0 / mm²
FOV1
FOV2
FOV3
FOV4
FOV5
FOV6
X̄=216.84; σ=52
X̄=156.09; σ=35
G
COVID-19
TMEM119
Haematoxylin
H
CTRL - PNEUMONIA
TMEM119
Haematoxylin

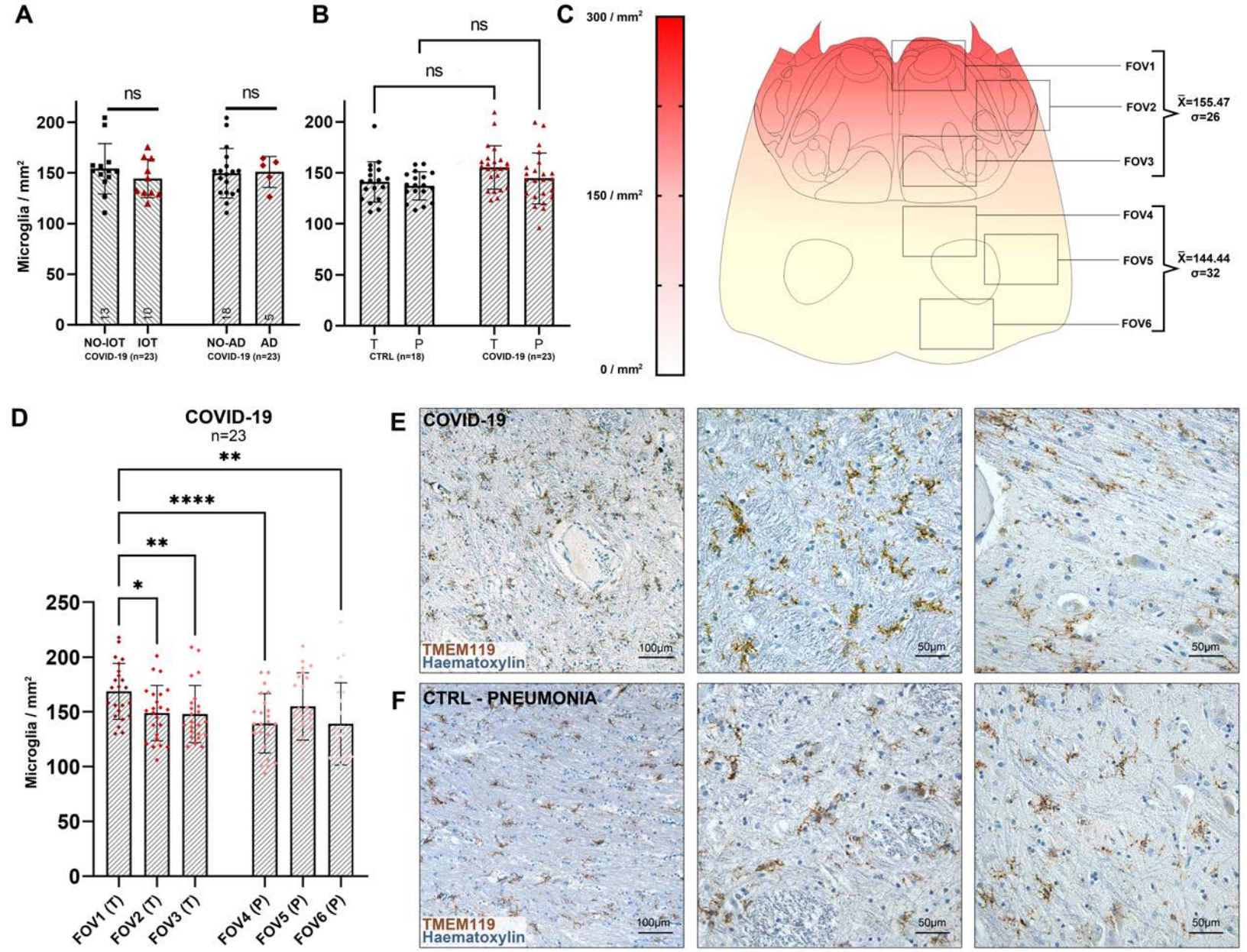
A
B
C
ns
ns
ns
Microglia / mm²
NO-IOT
IOT
NO-AD
AD
COVID-19 (n=23)
COVID-19 (n=23)
T
P
T
P
CTRL (n=18)
COVID-19 (n=23)
300 / mm²
150 / mm²
0 / mm²
FOV1
FOV2
FOV3
FOV4
FOV5
FOV6
X̄=155.47
σ=26
X̄=144.44
σ=32
D
COVID-19
n=23
FOV1 (T)
FOV2 (T)
FOV3 (T)
FOV4 (P)
FOV5 (P)
FOV6 (P)
E
COVID-19
TMEM119
Haematoxylin
100µm
50µm
50µm
F
CTRL - PNEUMONIA
TMEM119
Haematoxylin
100µm
50µm
50µm

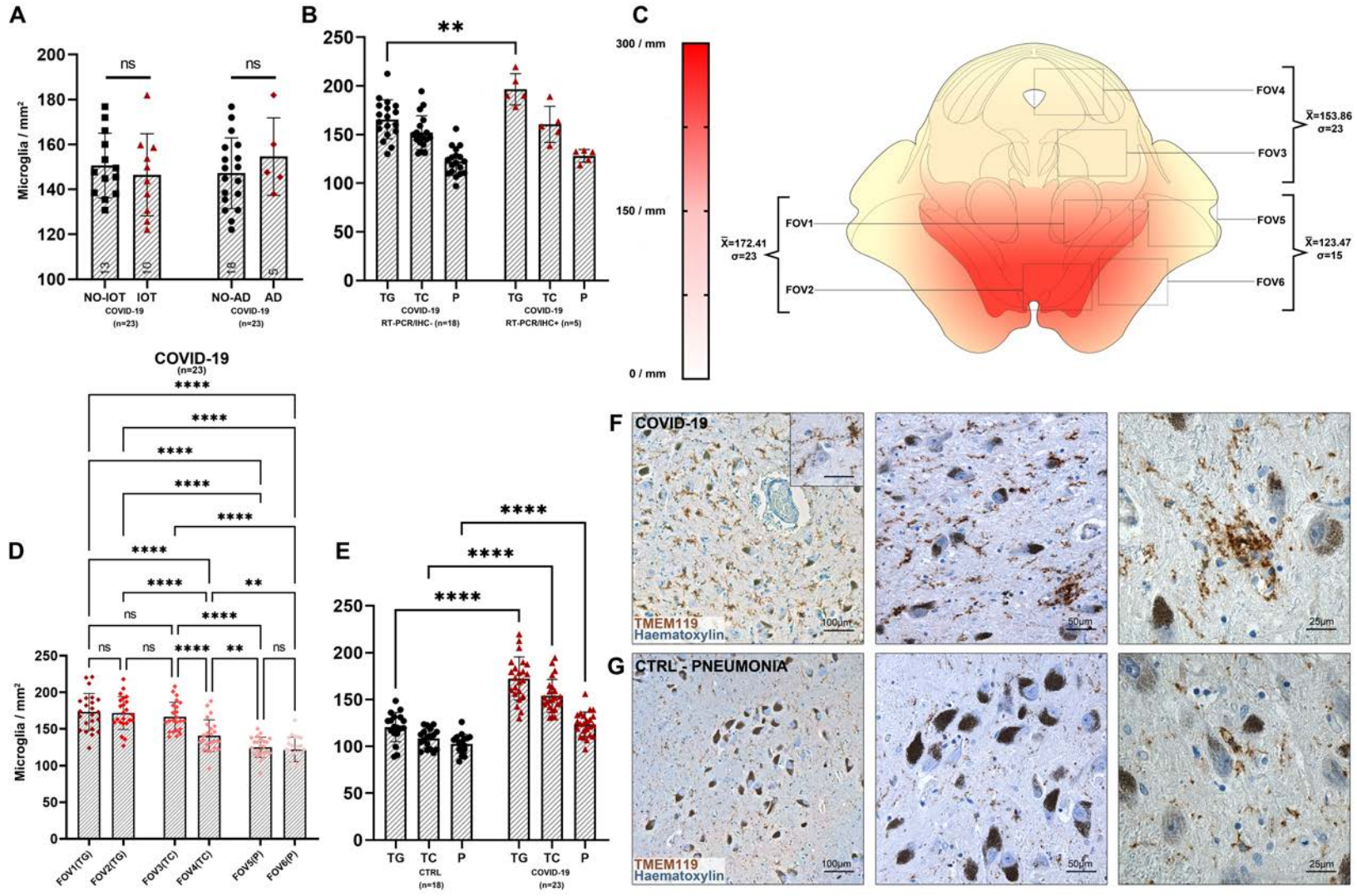
A
Microglia / mm²
ns
ns
NO-IOT
IOT
NO-AD
AD
COVID-19 (n=23)
COVID-19 (n=23)
B
**
TG
TC
P
TG
TC
P
COVID-19 RT-PCR/IHC- (n=18)
COVID-19 RT-PCR/IHC+ (n=5)
C
300 / mm
150 / mm
0 / mm
FOV1
FOV2
FOV3
FOV4
FOV5
FOV6
X̄=172.41 σ=23
X̄=153.86 σ=23
X̄=123.47 σ=15
D
COVID-19 (n=23)
FOV1(TG)
FOV2(TG)
FOV3(TC)
FOV4(TC)
FOV5(P)
FOV6(P)
E
CTRL (n=18)
COVID-19 (n=23)
F
COVID-19
TMEM119
Haematoxylin
100µm
50µm
25µm
G
CTRL - PNEUMONIA
TMEM119
Haematoxylin
100µm
50µm
25µm

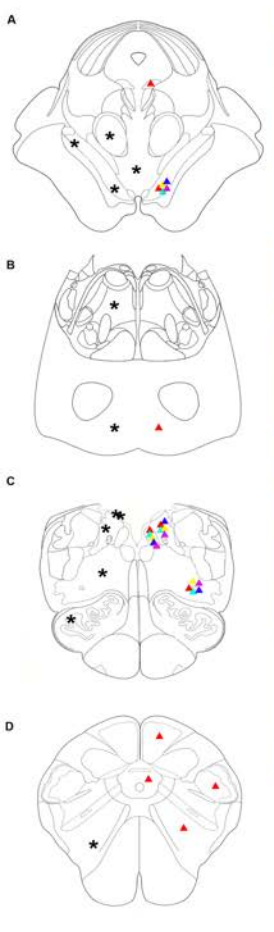

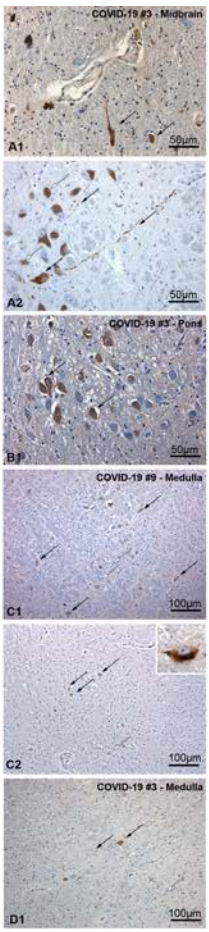

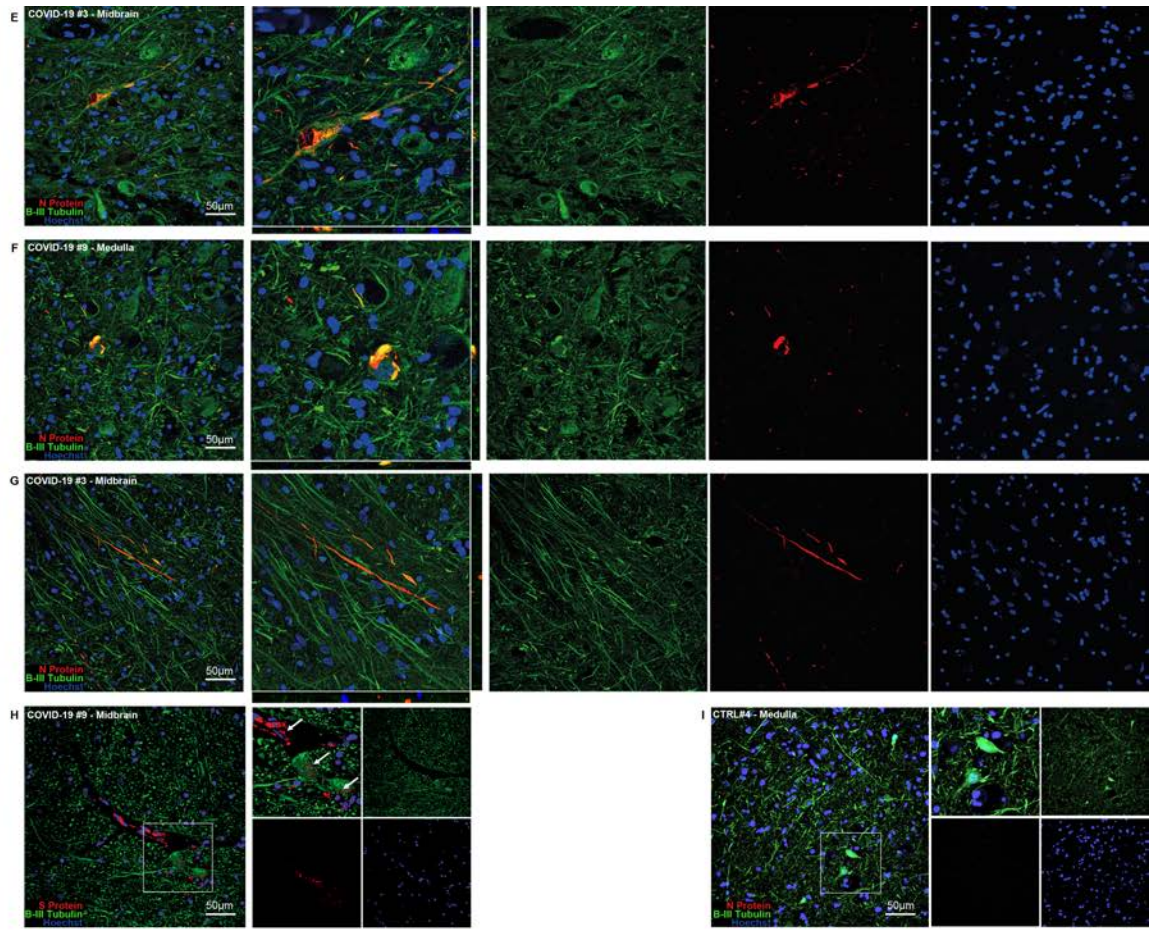

L) COVID-19 MEDULLA

	1	2	3	4	5	6	7	8	9	10	11	12	13	14	15	16	17	18	19	20	21	22	23	24
IHC - N	-	-		-	-	-	-	-			-	-	-	-	NA	-		-	-	-	-	-	-	-
IHC - S	-	-		-	-	-		-		-	-	-	-	-	NA	-		-	-	-	-	-	-	-
RT-PCR N Gene	-	-	32.30	-	-	-	35.49	-	37.40	-	-	-	-	-	NA	-	38.40	-	NA	NA	-	-	-	-
RNAseP	33.71	32.16	27.85	34.36	27.95	29.33	31.87	30.34	29.27	34.71	32.77	31.31	31.79	32.78	NA	30.73	26.95	27.39	NA	NA	30.71	32.78	31.12	29.34

M) COVID-19 MIDBRAIN

	1	2	3	4	5	6	7	8	9	10	11	12	13	14	15	16	17	18	19	20	21	22	23	24
IHC - N	-	-		-	-	-		-			-	-	-	-	NA	-		-	-	-	-	-	-	-
IHC - S	-	-		-	-	-		-		-	-	-	-	-	NA	-	-	-	-	-	-	-	-	-
RT-PCR N Gene	-	-	34.61	-	-	-	39.96	-	38.14	-	-	-	-	-	NA	-	-	-	NA	NA	-	-	-	-
RNAseP	33.41	29.28	29.43	31.33	26.81	29.42	31.42	31.36	28.81	36.07	31.44	34.27	29.74	32.62	NA	NA	27.75	27.21	NA	NA	32.53	31.67	30.69	29.15

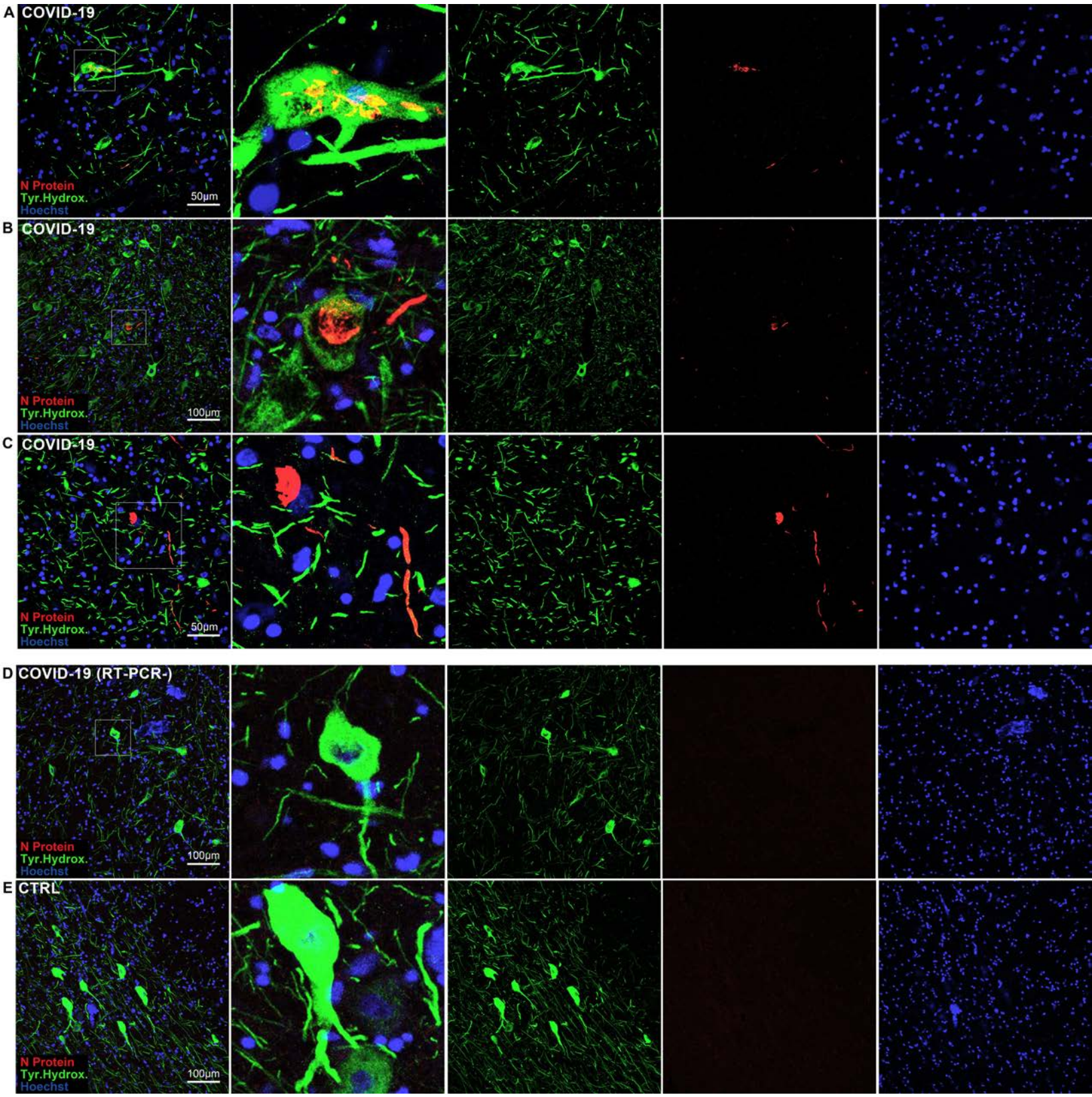
A
COVID-19
N Protein
Tyr.Hydrox.
Hoechst
50µm
B
COVID-19
N Protein
Tyr.Hydrox.
Hoechst
100µm
C
COVID-19
N Protein
Tyr.Hydrox.
Hoechst
50µm
D
COVID-19 (RT-PCR-)
N Protein
Tyr.Hydrox.
Hoechst
100µm
E
CTRL
N Protein
Tyr.Hydrox.
Hoechst
100µm

ID	Age	Sex	Hospitalization (days)	ICU	Intensive Oxygen Therapy	Anti-thrombotic medication	Steroid Medication	Hypertension	PMI	Antemortem Head CT	Neurological signs	Neuropathological evaluation	Brainstem Hypoxic Damage	Microthrombosis (NON-CNS)	Cause of Death
#1	87	F	2	N	N	Y	Y	Y	4	NA	Cognitive decline	AD neuropathological changes, CAA	Mild	Lungs, liver	Diffuse alveolar damage
#2	92	F	5	N	N	N	Y	N	1	NA	Cognitive decline, Alzheimer type	AD neuropathological changes, CAA	Mild	Lungs	Diffuse aveolar damage, intestinal infarction
#3	83	M	8	N	N	Y	Y	Y	2	Cerebral and cerebellar atrophy, chronic ischemic vascular disease	Frontoparietal ischemic insult (old) episodes of hepatic encephalopathy (HCV+)	Multi-infarct dementia, arteriosclerosis	Moderate	No	Diffuse alveolar damage, hepatic cyrrhosis
#4	97	F	9	N	N	Y	Y	Y	5	NA	Vascular dementia	Vascular dementia, arterioscelrosis, diffuse hypoxic/ischaemic damage	Mild	Lungs	Diffuse alveolar damage, cardiac amyloidosis
#5	78	F	15	N	N	Y	Y	Y	5	NA	NA	Early AD neuropathological changes, diffuse hypoxic/ischaemic damage	Mild	Liver	Pneumonia, aspergillus bronchopneumonia
#6	74	M	13	Y	Y	Y	Y	Y	4	Vascular calcification, expansive lesion of the right frontal lobe and right cerebellar hemisphere in patient with pulmonary neoplasia	NA	Small cell metastasic lung carcinoma with right cerebellar and frontal metastases	Mild	No	Small cell metastatic lung carcinoma, diffuse alveolar damage
#7	58	F	11	Y	Y	Y	N	N	2	Extensive ischaemic lesion of the territory of the right PCA, occulsion of the PCA	NA	Medial temporal lobe infarction	Moderate	No	Acute myocardial infarction, cardiogenic shock
#8	50	M	1	N	N	N	N	N	3	NA	NA	Arteriosclerosis, diffuse hypoxic/ischaemic damage	No detectable changes	No	Coronary atherosclerosis and myocardiosclerosis
#9	81	F	30	N	N	N	N	Y	3	Ischaemic regions in the MCA territory and diffuse cerebral and cerebellar atrophy due to chronic ischaemic vascular disease.	Soporous status	Mixed dementia with AD neuropathological changes, CAA and chronic ischemic vascular disease	Moderate	Lungs, liver	Atherosclerotic aortic aneurysm, pneumonia.
#10	60	M	30	Y	Y	Y	Y	N	3	NA	NA	Diffuse hypoxic/ischaemic damage	Mild	Heart	Pneumonia with emphysema.
#11	55	M	15	Y	Y	Y	Y	N	2	NA	NA	CNS microthromboses, haemorragic injury in the territory of the right MCA	Moderate	No	Pulmonary thromboembolism with infarcts.
#12	62	M	27	Y	Y	Y	Y	N	2	NA	NA	Arteriosclerosis, diffuse hypoxic/ischaemic damage	Mild	Lungs	Pneumonia with hemorrhages. Intestinal and hepatic infarcts.
#13	73	M	21	Y	Y	Y	Y	Y	2	NA	NA	Diffuse hypoxic/ischaemic damage	Moderate	No	Pneumothorax, Pneumonia, right pleurodesis,
#14	58	F	24	Y	Y	Y	Y	Y	1	Right anisocoria	No relevant signs	Diffuse hypoxic/ischaemic damage	Mild	Lungs	Pneumonia. Necrotic-haemorragic pancreatitis. Multiorgan failure.
#15	49	F	3	Y	Y	Y	N	N	2	Confusion and hallucinations; CSF Streptococcus Pneumoniae +	NA	Acute purulent meningitis, post-anoxic pathology	Moderate	No	Acute purulent meningitis. Post-anoxic cerebral death.
#16	72	M	10	Y	Y	Y	Y	Y	4	Hypostenia, dizziness, anosmia. Sudden fall.	NA	Diffuse hypoxic/ischaemic damage	Severe	No	Consolidative pneumonia. Hypertensive heart disease.

#17	72	M	38	N	N	N	Y	N	1	NA	NA	CNS microthromboses, extensive haemorragic injury of the right cerebellar hemisphere, ischaemic vascular disease	Mild	No	Multivascular obstructive coronary atherosclerosis. Left pulmonary infarct.
#18	82	M	6	N	N	N	Y	Y	3	Acute neurological event: Anisocoria, non responding	NA	CNS microthromboses, ischemic vascular disease	Mild	No	Lobar pneumonia
#19	40	F	1	N	N	NA	NA	Y	ND	NA	NA	CNS microthromboses, diffuse hypoxic/ischaemic damage	Moderate (medulla not sampled)	NA	Diffuse alveolar damage
#20	68	M	NA	N	N	NA	NA	Y	ND	NA	NA	CNS microthromboses, diffuse hypoxic/ischaemic damage	Severe (medulla not sampled)	NA	Diffuse alveolar damage
#21	73	M	5	Y	Y	Y	Y	N	5	NA	NA	CNS microthromboses, cortical and subcortical haemorrages, global ischaemia	Moderate	Lungs	Diffuse alveolar damage, Platelet/fibrin microthrombosis
#22	77	F	34	N	N	N	N	Y	5	No signs	NA	CNS microthromboses, ischemic vascular disease	Moderate to severe	Lungs	Chronic emphysema, diffuse alveolar damage and platelet/fibrin microthromboses.
#23	84	M	12	Y	Y	Y	Y	Y	4	Chronic ischaemic vascular disease	Cognitive decline	AD neuropathological changes, Parkinson's Disease, CNS microthromboses, ischemic vascular disease	Moderate	Lungs	Chronic emphysema, bacterial pneumonia, diffuse alveolar damage lung platelet/fibrin microthrombosis.
#24	89	F	1	N	N	N	N	Y	5	Chronic ischaemic vascular disease, territorial ischaemic injury (right occipital lobe, caudate nucleus and cerebellum)	Cognitive decline	AD neuropathological changes, CNS microthromboses, diffuse hypoxic/ischaemic damage	Moderate	Lungs	Chronic emphysema, diffuse alveolar damage and platelet/fibrin microthromboses

Table 1. Clinical data of the COVID-19 Group.

ID	Age	Sex	Hospitalization (days)	Hypertension	PMI	Antemortem Head CT	Neurological signs	Neuropathological evaluation	Brainstem Hypoxic damage	Microthrombosis (NON-CNS)	Cause of Death
#1	83	M	10	Y	5	Cerebral atrophy, Chronic ischaemic vascular disease	Cognitive decline	Mixed dementia with AD neuropathological changes ad chronic ischaemic vascular disease	Moderate	No	Pneumonia, respiratory insufficiency, ischaemic heart disease
#2	74	M	2	Y	4	Vascular calcification, ischaemic heart disease	NA	Chronic ischaemic vascular disease	Mild	No	Ischaemic heart disease.
#3	40	M	1	N	4	No signs	No signs	No detectable microscopical changes	No detectable microscopical changes	No	Haemorragic Shock
#4	79	F	31	Y	3	Cerebral atrophy, Chronic ischaemic vascular disease	Cognitive decline, Alzheimer type	AD neuropathological changes, CAA, ischemic vascular disease	Mild	No	Pentalobar pneumonia, respiratory insufficiency
#5	62	M	22	Y	5	NA	NA	Diffuse hypoxic/ischaemic damage	Mild	No	Pneumonia, respiratory insufficiency
#6	76	M	15	Y	6	NA	NA	Ischaemic vascular disease, diffuse hypoxic/ischaemic damage	Mild	No	Pneumonia, chronic ischaemic vascular disease
#7	75	M	12	Y	4	NA	NA	Diffuse hypoxic/ischaemic damage	Mild	No	Pneumonia, ischaemic heart disease
#8	78	F	8	Y	3	No	NA	Diffuse hypoxic/ischaemic damage	Mild	No	Pneumonia, ischaemic heart disease
#9	71	F	40	Y	3	NA	NA	Diffuse hypoxic/ischaemic damage	Moderate to severe	No	Acute respiratory failure, septic shock, peritonitis
#10	46	F	15	N	4	No signs	No signs	Diffuse hypoxic/ischaemic damage	No detectable microscopical changes	No	Respiratory insufficiency, multiorgan failure, cervical neoplasia
#11	75	F	20	Y	5	Chronic Ischaemic Vascular disease, Cerebral atrophy	NA	Vascular dementia, ischaemic vascular disease, diffuse hypoxic/ischaemic damage	Moderate	No	Pneumonia, acute respiratory failure, candidosis
#12	80	F	8	Y	4	Cerebral atrophy	Cognitive decline, Alzheimer type	AD neuropathological changes, diffuse hypoxic/ischaemic damage	Moderate	No	Pentalobar pneumonia, respiratory insufficiency
#13	81	F	NA	Y	3	NA	NA	Diffuse hypoxic/ischaemic damage	Mild	No	Pneumonia, acute respiratory failure
#14	63	F	NA	N	3	No signs	No signs	Diffuse hypoxic/ischaemic damage	Mild	No	Ischaemic heart disease
#15	70	M	38	Y	5	Chronic ischaemic vascular disease	NA	Ischaemic vascular disease, diffuse hypoxic/ischaemic damage	Moderate	No	Bilateral pneumonia, respiratory insufficiency.
#16	81	M	10	Y	4	Cerebral atrophy	Cognitive decline, Alzheimer type	Mixed AD neuropathological changes and Lewy Body pathology, diffuse hypoxic/ischaemic damage	Moderate	No	Pneumonia, respiratory insufficiency
#17	75	M	58	Y	6	Cerebral atrophy	NA	Vascular dementia, ischaemic vascular disease, diffuse hypoxic/ischaemic damage	Moderate	No	Pneumonia, respiratory insufficiency.

#18	87	M	30	Y	6	Cerebral atrophy	Cognitive decline	AD neuropathological changes, diffuse hypoxic/ischaemic damage	Moderate	No	Pneumonia, multiorgan failure.

Table 2. Clinical data of the Control Group